Influence of trains meeting on the ventilation performance of equipment compartment with independent air duct in high-speed train: numerical and

Railway Engineering Science (2025) 33(1):127–150
https://doi.org/10.1007/s40534-024-00355-3

Influence of trains meeting on the ventilation performance of equipment compartment with independent air duct in high-speed train: numerical and experimental study

Yitong Wu[1,2] · Wei Zhou[1,2] · Xifeng Liang[1,2] · Xinchao Su[1,2] · Kewei Xu[3] · Yutao Xia[1,2] · Zhixin Wang[1,2] · Sinisa Krajnović[3]

Received: 27 February 2024 / Revised: 18 July 2024 / Accepted: 18 July 2024 / Published online: 21 October 2024

Abstract

During the train meeting events, train equipment compartments are exposed to the worst pressure changes, potentially affecting the ventilation performance of equipment, particularly for electrical facilities equipped with independent air ducts. In this paper, a two-step method is used for numerical computation: (1) obtaining the temporal and spatial transient node data of the flow field sections during the train-passing simulation and (2) using the data as the input data for the equipment compartment simulation. In addition, this paper also compares the difference in equipment ventilation between the single-train and train-passing scenarios in real vehicle tests. The results indicate that the primary factors influencing ventilation effectiveness are the aerodynamic compression and deceleration of airflow induced by the other train's nose, as well as the instability of the external flow field in the wake of the other train. During train crossing, the air is forced into the air duct, with a maximum ratio of the airflow in-duct to the airflow out-duct reaching 3.2. The average mass flow falls below the rated mass flow for the converter. Compared to the rated air volume of converter, the maximum suppression rates obtained from testing and simulation are –24.5% and –16.8%, respectively. Compared to the single-train operation, the maximum suppression rates obtained from testing and simulation are –15% and –18%, respectively. These findings provide valuable insights into the design and operation of high-speed trains.

Keywords Train-passing event · Electrical facilities · Independent air duct · Ventilation performance

List of symbols

Abbreviations

AD	Air duct inside the electrical equipment
CFL	Courant-Friedrichs-Lewy number
FS	Free sides of two trains
HST	High-speed train
IDDES	Improved delayed detached eddy simulation approach
LES	Large eddy simulation method
MS	Meeting side of two trains
NHC	Equipment compartment of the 2nd car simulation case
NTC	Equipment compartment of the 7th car simulation case
RNG	Re-normalisation group method
SST	Shear stress transport method
SIMPLE	Semi-implicit method for pressure-linked equations

✉ Wei Zhou
zhou_wei000@126.com

✉ Xinchao Su
suxinchao@csu.edu.cn

[1] Key Laboratory of Traffic Safety On Track, Ministry of Education, School of Traffic and Transportation Engineering, Central South University, Changsha 410075, China

[2] Joint International Research Laboratory of Key Technology for Rail Traffic Safety, Central South University, Changsha 410075, China

[3] Division of Fluid Dynamics, Department of Mechanics and Maritime Sciences, Chalmers University of Technology, SE-41296 Gothenburg, Sweden

T1HN	Head nose of train 1
T2HN	Head nose of train 2
T1-2	Location of P2-1 on the 2nd car of train 1
T1-7	Location of P7-1 on the 2nd car of train 1
T1TN	Tail nose of train 1
T2TN	Tail nose of train 2
TS	Single-train stationary condition
TR	Single-train operation condition
TP	Train-passing events
TTPT	T-Typed pitot tube
URANS	Unsteady Reynolds-averaged Navier-Stokes method

Parameters

L	Length of the train (m)
H	Height of the train (m)
W	Width of the train (m)
V_i	Simulation region moving velocity, and i represents the region number (m/s)
Ma	Mach number
x, y, z	Coordinate system of streamwise, lateral, and vertical directions
u, v, w	Instantaneous velocity in the x, y, z components (m/s)
U_o^*	Normalised velocity magnitude relative to moving region of train meeting simulation
U_r^*	Normalised velocity magnitude relative to static region of equipment cabin simulation
ΔP	Pressure loss (Pa)
ρ	Air density (kg/m^3)
U_s	Airflow velocity magnitude on the surface (m/s)
α	Porous inertial resistance
β	Porous viscous resistance
$y+$	Non-dimensional distance of the first grid node to the wall surface
Δt	Physical time step (s)
Pi'(i')-i''	Pressure probes, i'(i') represent the first (last) 4 cars' carriage number of the train, i'' represents the probe number on each carriage
Vi' (i')-i''	The velocity probes, i'(i') represent the first (last) 4 cars' carriage number of the train, i'' represents the probe number on each carriage
C_{p_max}, C_{p_min}, ΔC_p	Maximum, minimum, and peak-to-peak values of the pressure coefficient
t_i	Physical time, i represents the special time during train meeting event (s)
C_p	Pressure coefficient
U_h^*	Normalised velocity in the horizontal plane
u^*, v^*, w^*	Normalised instantaneous velocity in the x, y, z components
U_v^*	Normalised velocity in the vertical plane
ΔP_d	Dynamic pressure (Pa)
V_m	Measured airflow velocity (m/s)
Q	Air volume (m^3/h)
V_{mi}	Measured velocity, i represents the measurement point number (m/s)
S	Area of the air outlet vent cross section (m)
c_{q_sim}	Normalised averaged air volume of the simulation
c_{q_test}	Normalised averaged air volume of the real vehicle test
Q_{static}	Average air volume during the train is static (fans are working) (m^3/h)
Q_{TP}	Average air volume during the train-passing event (m^3/h)
Q_{rated}	Rated air volume of the ventilation equipment's cooling fan (m^3/h)

1 Introduction

As a green transportation mode, high-speed trains (HSTs) are poised to become a popular transportation choice in the future. Consequently, the frequency of HST services is expected to increase, leading to a corresponding rise in instances of train encounters. When two trains pass by each other, significant transient pressures occur [1]. Chen and Wu indicated that each train is subjected to 6 times directional changes in the shaking force moment and impact force moments during the train meeting period [2]. The yaw and overturning moments resulting from the train meeting event can seriously affect the train's running safety [3]. To mitigate the adverse effects of the impulsive load, the operation speed of the HST is restricted [4]. These unsteady impulsive aerodynamic loads also occur in situations when a single train passes over noise barriers [5–7], train stations [8–11], tunnel [12–14], human bodies [15, 16], and when two trains meet on the bridge [17, 18], under crosswind [19–21], or inside tunnels [22–24]. The unsteady impulsive aerodynamic loads are extremely hazardous to the operational stability of the train and to the safety of surrounding objects [25].

To ensure the safety of trains and surrounding objects, many scholars have investigated the fundamental nature and

influencing factors of the impulsive load. Raghunathan et al. reported that when the head cars pass each other, a positive–negative pressure pulse wave is generated [26]. When the tail cars meet, a negative–positive pulse pressure wave is induced. The peak pressure produced by the train meeting event is proportional to the square of the speed of trains, and the time width of the peak pressures is proportional to an inverse of the sum of the trains' speeds. The values of the peak-to-peak pressure coefficient for the train meeting event are approximately double that of a single-train moving [27]. The studies of impulsive load characteristics contribute to developing safety standards for buildings near trains and passengers at the station. Piecewise linear representation techniques are used to recharacterise typical high-dimensionality pulse pressure waves [28]. It provides a novel processing method for main trend extraction and dimensionality reduction of the pulse pressure wave data. Tian and He conducted the factors affecting the air pressure pulse generated by the train meeting event based on a series of moving model tests and numerical calculations [29]. An assessment with consideration of operational safety was proposed, and the limiting pressure loads that can be sustained by the train body and windows were determined. Baker et al. reported a series of experiments using a moving model train to investigate the nose pressure pulses of trains and their effect on trackside structures, which supplemented the obsolete measurements and calculations data in Eurocode [30].

The large pressure changes during the train meeting event can be transmitted from gaps in the train body to the interior of the train, resulting in transient pressure changes inside the passenger cabin [31]. The pressure changes seriously impaired passenger comfort for the train with unfavourable airtightness [32]. When the pressure transmission from the train surface into carriages reaches 800 Pa/s, the pressure may cause damage to the eardrum, resulting in the hearing loss of the train driver [33]. When a train passes through a tunnel, the pressure changes inside and outside the train have a more significant impact on the train and the human body due to the blockage rate [34]. Sun et al. [35] studied the pressure variations inside and outside trains with different airtightness indices. Based on the corresponding criteria for different airtightness indices, the critical tunnel diameters corresponding to different train operating speeds were determined.

Moreover, the adverse effect of the train meeting event is also reflected in the flow field around the train. The shape of the inter-car gaps and the configuration of the bogies might influence the growth of the boundary layer thickness when two trains encounter [30]. The train meeting event can also cause complicated airflow changes with high slipstream velocity [36, 37]. Li et al. [38] found that the absolute maximum value of the longitudinal velocity component is approximately 9 times greater than the transverse and vertical components for the train meeting inside the tunnel. Meng et al. [39] reported that a pair of counter-rotating longitudinal vortices followed by the near wake region of trains intersect in the train meeting period, enhancing the intensity of the turbulence in the flow field around trains. Especially, the effect of the train meeting event on the flow field occurs mainly at the bottom of either side of the train.

The above studies have contributed to the safety of train operations by examining in detail the temporal and spatial pressure fluctuations and airflow structure variations of train meeting events under different scenarios. Fluctuations in pressure and airflow around the train can also influence the ventilation performance of the equipment. Before discussing the studies concerning the equipment compartment of HSTs, there are some studies on the ventilation performance of equipment compartments of other delivery vehicles, such as aeroplanes and missiles. Yi et al. [40] developed a temperature field analysis method based on the ANSYS parametric design language for investigating the heat dissipation issues of the high-speed missile's cabin. Wang et al. [41] proposed an improved multi-nozzle spray cooling method for controlling the temperature of most equipment surfaces inside the aircraft equipment cabin. These studies can be used as references for investigating the ventilation performance of equipment compartments in HSTs. Niu et al. [42] investigated the indoor flow field of a dedusting equipment cabin in tunnels. The effects of different air intake locations on the airflow rate of the cabin's filter cartridges are compared. Nevertheless, the effects of filter cartridge parameters and the fan performance are not considered in this study. Jia et al. [43] studied the surface temperatures of the equipment when the HST is running in the open air in the summer. They indicated that the equipment at two ends of the equipment compartment has unfavourable ventilation performance with the highest temperature of 81.9 °C, due to the train changing the operation direction. Zhang et al. [44] studied the surface temperatures of the equipment when the train passed through a windy area with an ambient temperature of 45 °C and a crosswind speed of 20 m/s. They found that the maximum temperature could reach 89 °C at the top of the converter of the head car. Li et al. [45, 46] worked on the condensing air flux performance of air-conditioning on the top of the HST. They concluded that the interaction of the airflow through the air-conditioning units and the boundary layer on the roof of the train resulted in a significant drop in the condensing air flux. Wu et al. [47] adopted the improved delayed detached eddy simulation (IDDES) approach and *T*-typed pitot tube (TTPT) measurement devices to investigate the ventilation performance of equipment with independent air ducts when a single train operates in the open air. They found that the equipment ventilation effect of the independent air duct in Alpine

HST is directly influenced by the external environment. These studies on the ventilation performance of equipment in the train were based on the single-train scenario. The influences of the train meeting event on the ventilation characteristic of the equipment compartment have not been studied. Considering the more drastic changes in the environmental pressure fluctuation and airflow variation caused by the train meeting event, the influence of the train meeting event on the ventilation characteristics of the equipment compartment with the independent air ducts needs to be studied.

For these reasons, this work aims to clarify and investigate the ventilation characteristics of electrical facilities and equipment compartment with the independent air ducts in the train meeting event using numerical calculations and real vehicle tests. Specific contributions of this work are as follows:

1. A two-step simulation method is used to obtain the node data of the spatial–temporal transient mapping on the flow field cross sections during the train meeting process, which is used as an input to the simulation of the equipment compartment region, and thereby captures the details of the flow characteristics around the equipment compartment more economically.
2. The effects of the ventilation equipment inside the electrical facilities on the overall ventilation performance of the equipment compartment are considered, giving a more realistic representation of the ventilation characteristics of the equipment compartment.
3. The transient and continuous influence of train meeting event on the overall ventilation performance of the ventilation equipment is characterised, to provide recommendations for the ventilation equipment design.
4. The spatial effect of marshalling locations in the train meeting event on the ventilation performance of equipment compartments is performed, advising on the ventilation equipment arrangement.
5. *T*-type pitot tubes (TTPTs) are adopted in the airflow measurement of a real vehicle test. The TTPT is a bendable and miniature pitot tube that enables multiple measuring points to be installed at a limited area of ventilation air vents.

2 Methodology

2.1 Geometry models

2.1.1 Alpine HST model

As a result of an increased demand for train transport in China, both the number of trains and the length of train formations are expected to increase. The train formation is usually 8 cars, 16 cars, or even longer. Jiang et al. indicated that the grouping length of the train has a significant influence on the slipstream velocity and the pressure waves [48]. Tan et al. found that with the increase in the marshalling length, the position of the flow separation in the tail car is advanced [49]. When long marshalling trains meet, the impact on the ventilation effect on the equipment compartment of each car may be repeated and continuous. Hence, a full-scale operating Alpine HST model with 8 cars is used for both the numerical simulation and the real vehicle test in this study. The length (L), height (H), and width (W) of the train are 201.39, 3.86, and 3.33 m, respectively. As shown in Fig. 1, the details of bogies are retained, and the pantographs of the train and rail models are not included in this simulation.

2.1.2 Equipment compartment model

The head and the tail cars are trailers without electrical facilities in the equipment compartments. Therefore, the equipment compartments in the 2nd car and 7th car are chosen for the research objects in this study. The equipment compartments of these two cars have the same internal arrangement, with two dust collection airboxes, a water tank, a transformer, and a converter as shown in Fig. 2. The length, width, and height of the equipment compartment are 4W,

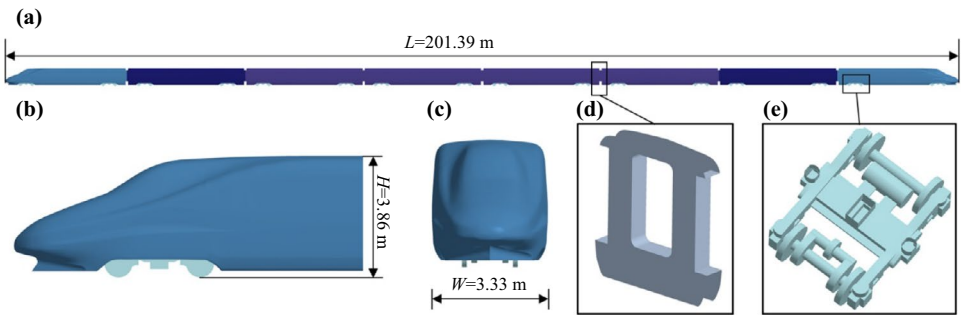

Fig. 1 **a** Side view, **b** head car, **c** front view, **d** interior gap and **e** bogie of the 8-marshalling Alpine HST model

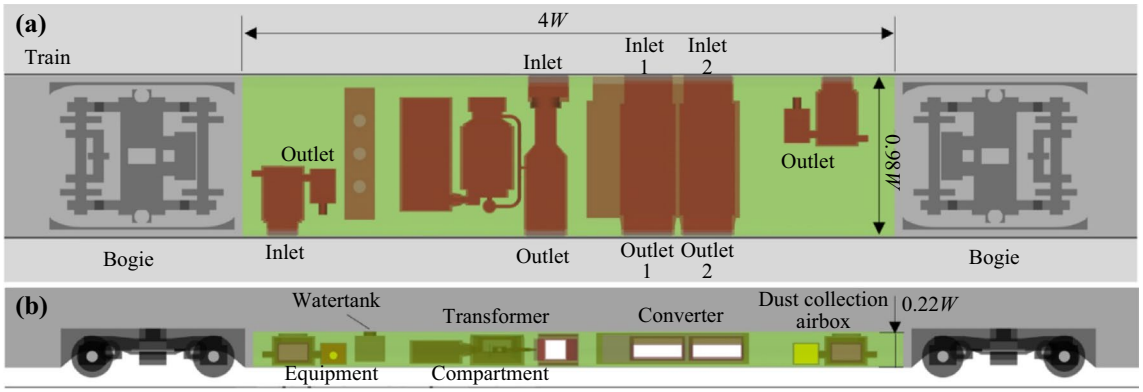

Fig. 2 **a** Top view and **b** side view of the equipment compartment and electrical facilities

0.98W, and 0.22W, respectively. The ventilation facilities of Alpine HST use the independent air duct to prevent the spread of sand in the equipment compartment. The air inlet and outlet vent are connected by deflector shields and air ducts. Besides, the ventilation fans are mounted inside the air duct, forcing the air to flow in and out from the equipment. A grille and filter are installed at each air vent to smooth the train surface and screen out impurities.

2.2 Numerical method

The unsteady re-normalisation group (RNG) k-ε turbulence model implemented in the Reynolds-averaged Navier–Stokes (URANS) method was found to be an effective model to simulate the pressure fluctuation caused by trains passing each other in open air [27] or tunnels [22, 38, 50]. Hence, the URANS method is used in the train meeting simulation. However, the URANS method would ignore turbulent fluctuations, and conversely, the IDDES approach has been validated to capture the instantaneous flow field around the HST simulation [51–54], the indoor ventilation simulation [55], and the wake flow investigation [56–58]. To obtain a more precise characterisation of the flow field around the equipment compartment, the IDDES method is used in the equipment compartment simulation.

IDDES, a hybrid modelling approach, integrates the advantages of RANS and large eddy simulation (LES) methods. Its fundamental principle is to utilise the RANS resolution in the near-wall region to reduce computational expenses while maintaining LES accuracy in resolving the flow separation and other complex flow phenomena. For the RANS portion, the shear stress transport (SST) k–ω turbulence model is often chosen due to its capability to handle adverse pressure gradient flows and its independence from free stream conditions [59]. The governing continuity and momentum equations are discretised using a commercial finite volume solver STAR-CCM + . Convective fluxes are discretised using a hybrid upwind scheme, blending the second-order upwind scheme typical in RANS with central differencing favoured in LES. The second-order implicit scheme is used for the temporal advancement and the time derivative discretisation for unsteady flow calculations. The semi-implicit method for pressure-linked equations (SIMPLE) algorithm is used to update the pressure and velocity fields.

2.3 Computational domain and boundary conditions

2.3.1 Train meeting simulation

A sliding mesh method is adopted to simulate the relative motion between two trains. The sliding mesh method has been proven to be one of the most effective ways of simulating the relative motion of train meeting event [60]. The computational domain is divided into three regions: region 1 with the moving velocity V_1 (− 55.56 m/s), region 2 with the moving velocity V_2 (55.56 m/s), and a stationary field, region 3 around the two regions, as shown in Fig. 3a. The relative velocity of trains reaches 111.12 m/s, leading to the Mach number (Ma) reaching 0.32, which can be assumed to be compressible when $Ma > 0.3$ [61]. Region 1 and region 2 contain one train inside. The noses of two trains with an initial distance of 0.5L ensure a relatively stable flow field at the beginning. The coordinate system is denoted by x, y, and z for the streamwise, lateral, and vertical directions, respectively. Its origin is at the bottom of the wheel on the vertical centreline where the two trains meet. Conventional notations for the x, y, and z components of the instantaneous velocity field are denoted by u, v, and w, respectively. The superscript asterisk * is used to mark the normalised quantities. Reference values are the train width W and the region motion velocity. The tail nose of the train is 0.6L from the inlet of region 3. The lengths of regions 1, 2, and 3 are 5.4L,

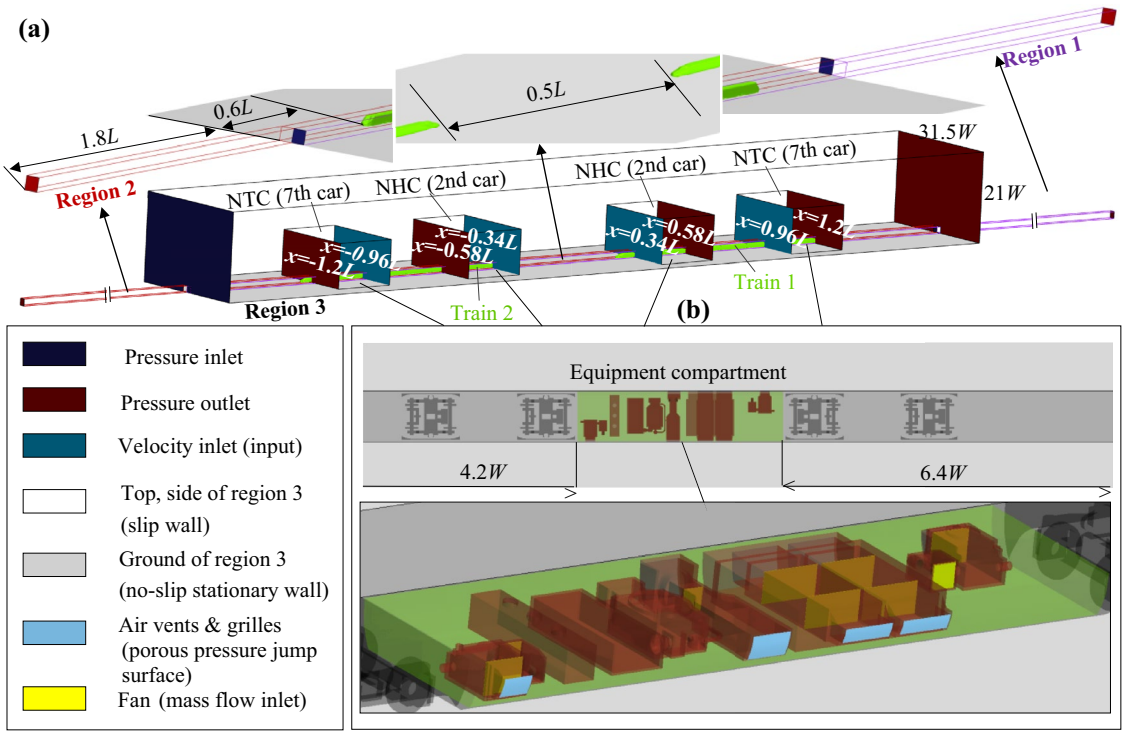

Fig. 3 Computational domain of **a** the train meeting simulation and **b** the equipment compartment simulation

5.4L and 3.6L, respectively, which are long enough to avoid the wake structure of two trains when they were passing by each other. The cross section of regions 1 and 2 is a square with a side length of 1.32W. So, the distance of two trains in the y-direction is 1.32W. The width and height of region 3 are 31.5W and 21W. The ground clearances between the train and region 1/2 and between region 1/2 and region 3 are 0.1 m. The inlet and outlet of the three regions are set as pressure inlet and pressure outlet, respectively. The top and sides of region 3 are set as slip walls. A no-slip stationary wall is set for the rest planes. The inlets of regions 1 and 2 are aligned with the inlet and outlet of region 3, respectively. Three pairs of interfaces are established for data exchange and relative motions realising: interfaces of region 1 to region 3, region 2 to region 3, and region 1 to region 2, as shown in Fig. 4.

2.3.2 Equipment compartment simulation

Since the aerodynamic characteristics of the two trains are identical when they pass by each other at the same speed [62], the next discussion and analysis will focus on Train 1. The equipment compartment simulations of the 2nd car and 7th car are denoted as a near head car (NHC) and near tail car (NTC) condition. The calculation domain of the equipment compartment simulation is shown in Fig. 3b; the length, width, and height of the computational region are 15W, 21W, and 11W, respectively. The ground clearance of the train is 0.2 m. For the NHC condition, the length region is located from $x = 0.34L$ to $x = 0.58L$ of the train meeting simulation. For the NTC condition, the length region is from $x = 0.96L$ to $x = 1.2L$. The origin of the equipment compartment simulation is at the bottom of the wheel on the vertical centreline of Train1. The spatial–temporal transient mapping velocity distributions on the inlet surfaces near the 2nd car and 7th car taken from the simulation results of the train meeting simulation are applied as boundary conditions, respectively. The velocity inlet of the NHC and NTC condition is obtained from the cross-sectional plane on $x = 0.34L$ and $x = 0.96L$ of the train meeting simulation, respectively. The velocity magnitude relative to the moving region obtained from the train meeting simulation is denoted as U_o^*. The train is stationary in the equipment compartment simulation; the inlet surface and ground plane are given a velocity to simulate the train motion. The velocity magnitude relative to the static region input on the inlet surface is denoted as U_r^*. The ground is a no-slip moving wall with a speed of 55.56 m/s. The lateral and upper walls are set as slip walls. A zero-pressure outlet is set as the boundary condition of the outlet end. The effect of ambient wind and temperature is not considered in this simulation. The fans mounted in the inlet and outlet of the air duct inside the dust collection airbox and converter, and

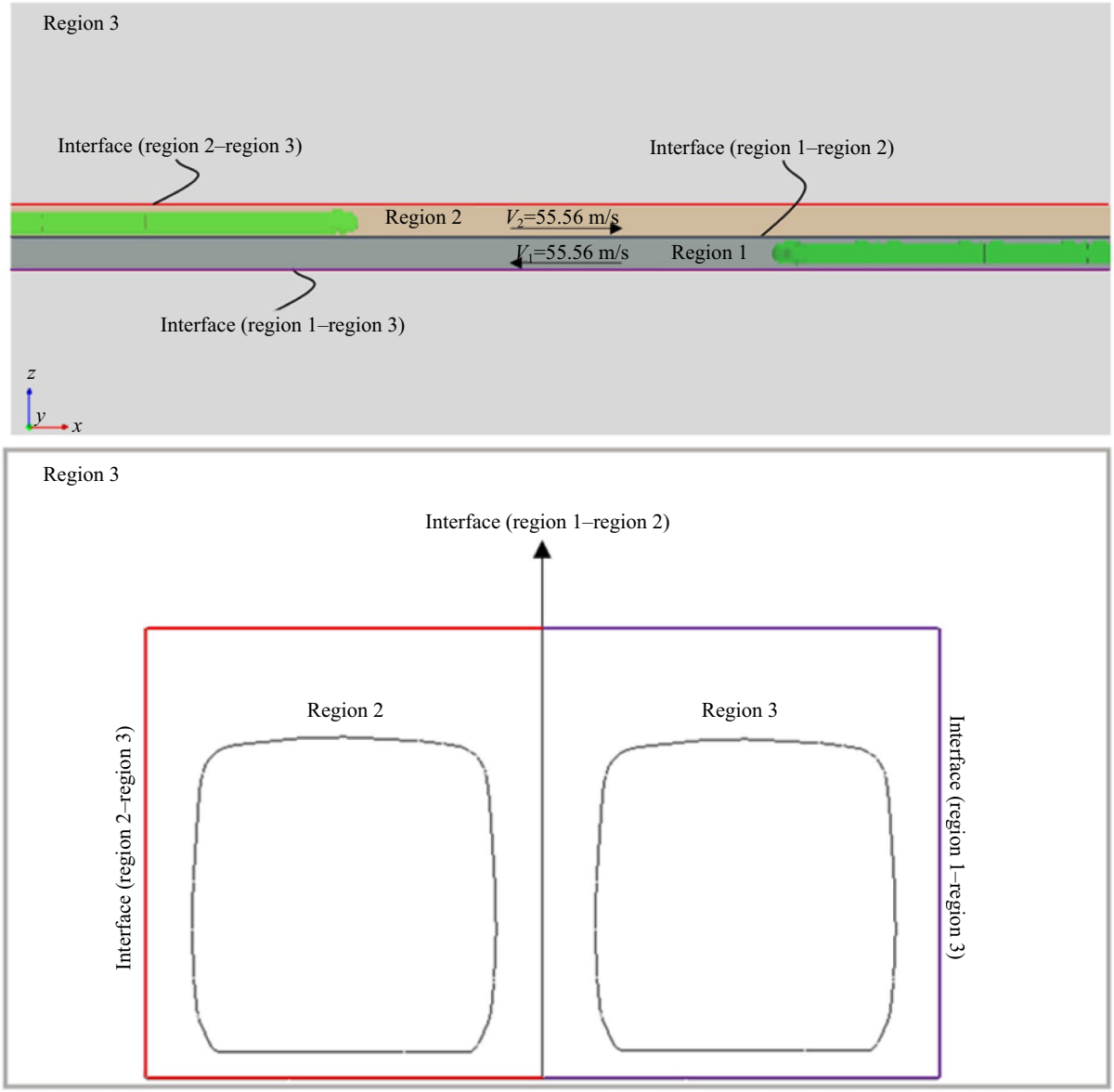

Fig. 4 Interfaces of the train meeting simulation

the inlet of the transformer are set as mass flow inlet boundary conditions. The airflow direction of the fans in the inlet vent (denoted as extractor fan) is from the external environment to the air duct, and the direction of the fans in the outlet vent (denoted as exhaust fan) is from the air duct to the external environment. The mass flow rates of the extractor fan in the duct collection air box, the transformer, and the converter are 1.8375, 3.0625, and 1.3271 kg/s, respectively. The mass flow rates of the exhaust fan in the duct collection air box and the converter are 1.021 and 0.79625 kg/s, respectively [63]. The grilles and filter are simplified as porous pressure jump surfaces in this simulation, and the pressure loss caused by them is calculated according to Eq. (1) [64].

$$\Delta P = \alpha \cdot \rho \left| U_s \right|^2 + \beta \cdot \rho \left| U_s \right|, \tag{1}$$

where ΔP is the pressure loss (Pa); ρ is the air density, 1.225 kg/m^3; U_s is airflow velocity magnitude on the surface (m/s); α is the porous inertial resistance; β is the porous viscous resistance. Here, the α is equal to 0.42996 and β is equal to 4.27159.

2.4 Mesh strategy

2.4.1 Train meeting simulation

The trimming and prism layer mesh methods are used. The first-layer thickness is 0.37 mm with a growth factor of 1.2, and 12 prism layers are produced to solve the boundary on the wall surface. The average surface mesh size of the bogies and train is 0.0296 and 0.0592 m. The average mesh sizes of regions 1, 2, and 3 are 0.227, 0.227, and 0.474 m. The grid construction around the train is shown in Fig. 5. The overall number of computational cells is 56.8 million. The wall y + on surfaces of the middle cars are around 20, and the head and tail car are lower than 30 during the train meeting period, which satisfies the requirement of the target wall $y+$ value, $1 < y+ < 30$, based on the unsteady RNG k-ε turbulence model with enhanced wall treatment. It combines a two-layer model with enhanced wall functions [65]. The physical time step is $\Delta t = 5 \times 10^{-4}$ s with 30 iterations in each time step, which ensures the CFL number is lower than 1 in around 99% of the cells in the interest region. The total computational time is 4.8 s, which ensures two trains have passed by each other.

2.4.2 Equipment compartment simulation

The same mesh method as the train meeting simulation is used, and the first-layer thickness of 0.21 mm and 12 prism layers is applied. The average mesh size of the equipment surface is 0.0168 m. The average mesh size of refinement areas around the equipment and cabin region is 0.0336 m and 0.0672 m, as shown in Fig. 6. The overall number of computational cells is 21.5 million. The average value of wall $y+$ on surfaces of train, equipment compartment, and facilities is lower than 10, and the wall surfaces of air ducts are lower than 30, which satisfies the requirement of the target wall $y+$ value is $1 < y+ < 30$ based on the IDDES model with hybrid wall functions [66]. The physical time step of the transient calculation is $\Delta t = 5 \times 10^{-4}$ s, which ensures the CFL number is lower than 1 in around 99% of cells in the

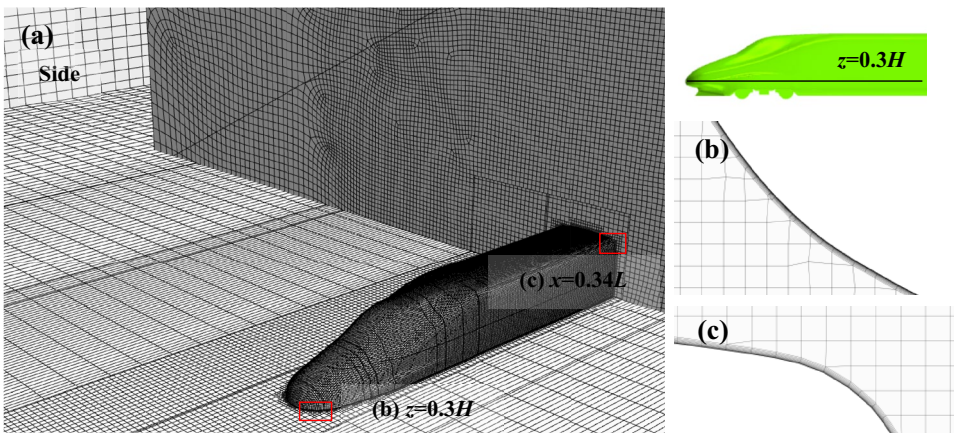

Fig. 5 Grid construction of **a** the train meeting computational region, **b** the train nose area on the plane $z = 0.3H$, and **c** the plane $x = 0.34L$

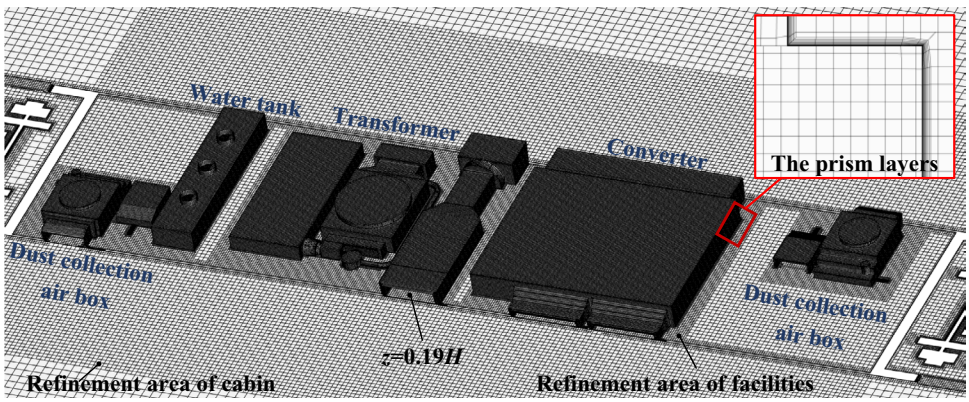

Fig. 6 Grid construction details of the equipment compartment area on the plane $z = 0.19H$ and surface of electrical facilities

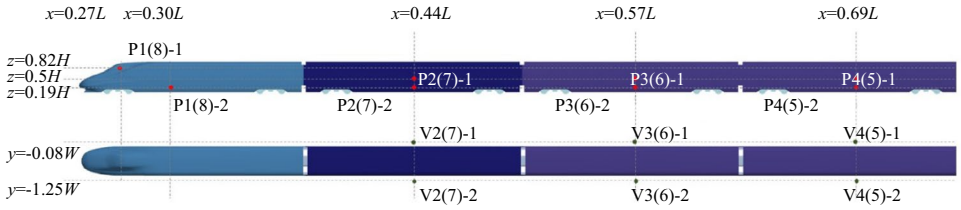

Fig. 7 Measurement probes arrangement of the train meeting simulation

interest region. The maximum number of inner iterations for each time step is 10. The total computational time is 4.8 s. Since the grid resolution of this simulation is the same as the medium mesh case in Ref. [47], no further grid-independent study is conducted here.

3 Results and discussion

Several measurement probes are arranged in the train meeting simulation, as shown in Fig. 7. The red points represent the pressure probe on the train surface, and the green points represent the velocity probe on two sides of the train. There are two pressure probes (Pi' (i')-i'') in each car and two velocity probes in the 2nd car and 7th car (Vi'(i')-i''). Due to the symmetrical properties of the train, the carriage number of the first 4 cars is denoted as i', the last 4 cars' number is denoted as (i'), and the probe number in each carriage is denoted as i''. The line $y=-0.08W$ is located at the meeting side, and the line $y=-1.25W$ is located at the free sides of the two trains.

3.1 Method validation

Xiong and Liang performed a real vehicle test in 2006 in China. Two CRH2 HSTs were passing by each other at the same speed of 200 km/h [67]. The test lines are the section of straight multiple railway lines with a spacing of 4.4 m. The test system comprised pressure measuring sensors, an amplifier, an A/D converter, a PC, and data collecting and processing devices. This system has a high resolution of the measured signal. By analysing and processing the transient pressure signals measured in real-time, the system effectively eliminates noise interference, accidental errors, and systematic errors, achieving high accuracy of the measurement results. The piezoresistive pressure sensors (8515C-15 produced by ENDEVCO) with a maximum measurement range of 103.35 kPa were used in this test. It has high measurement accuracy and minimal influence on the flow field. By mounting them on the meeting side of two trains, the dynamic pressure curves of the train surface during the train meeting period can be obtained. The sampling frequency is 1 kHz in this test.

To validate that the simulation method is suitable for the train meeting event, the pressure coefficient measured by pressure sensors P2-1 on the middle of the 2nd car in this simulation was compared with a real vehicle test. The maximum, minimum, and peak-to-peak values of the pressure coefficient caused by the head car passages are denoted as C_{p_max}, C_{p_min}, and ΔC_p, respectively. As shown in Fig. 8, the ΔC_p of the test and simulation is 0.336 and 0.347, respectively, showing good agreement.

Moreover, the reliability of the two-step method needs to be validated. Based on the previous study in ref. [47], the difference in simulation results between the two-step method and the conventional coupled simulation method (the whole

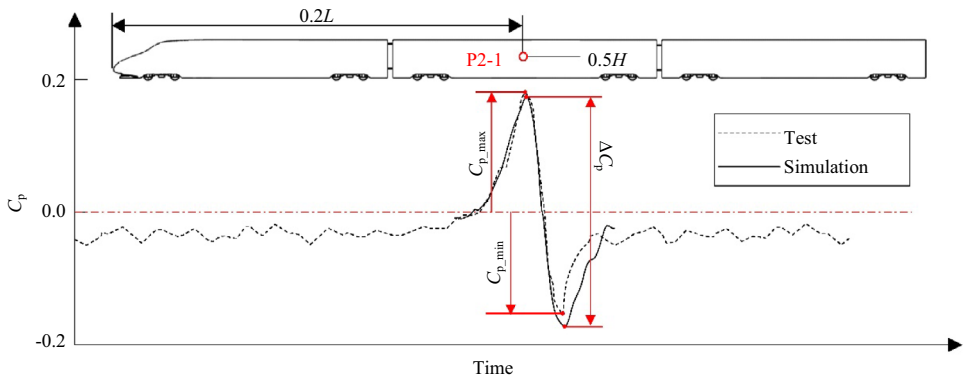

Fig. 8 Pressure coefficient history curves of the P2-1 during the train meeting event in the real vehicle test and simulation

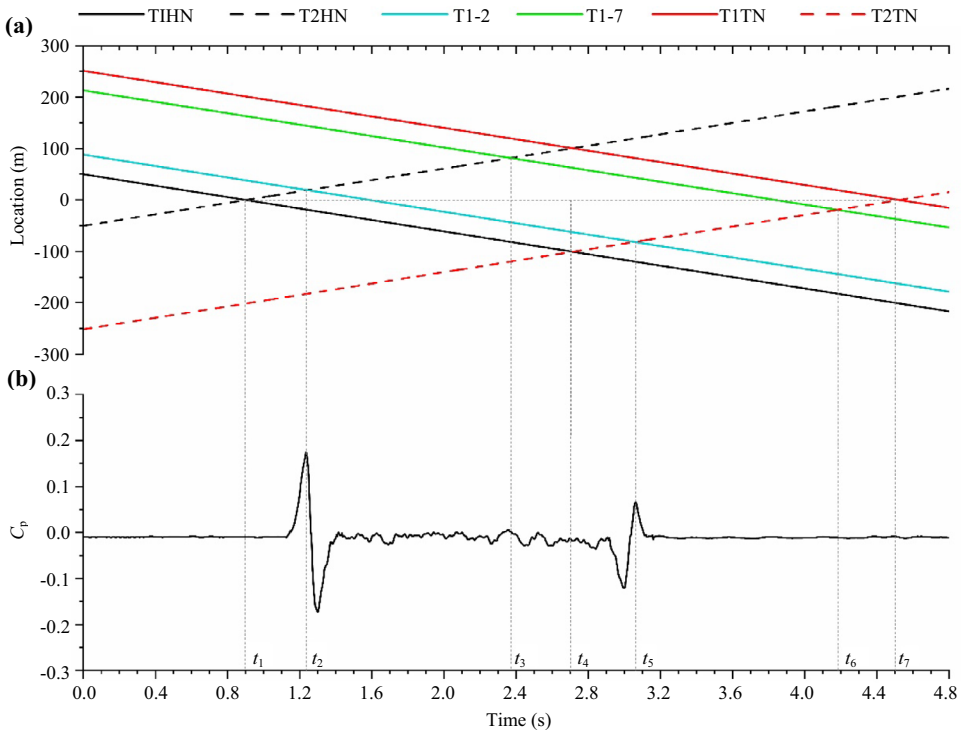

Fig. 9 **a** Operation map and **b** the time history pressure coefficient curve on the measuring point during the train meeting event

train model with the equipment compartment and electrical facilities) when a single train running in the open air was evaluated. The two-step method can capture similar fluctuation and values in the flow field around the train compared to the coupled simulation method. Moreover, the CPU solver time per time step of the two-step method was reduced by 62%.

3.2 External field

In this section, the external field of two trains passing by each other is analysed. The operation map of two trains is shown in Fig. 9a, which illustrates the time history location of the head nose of train 1 (T1HN), the head nose of train 2 (T2HN), P2-1 on the 2nd car of train 1 (T1-2), P7-1 on the 7th car of train 1 (T1-7), the tail nose of train 1 (T1TN), the tail nose of train 2 (T2TN). Based on the operation map, some special moments during the train meeting period which are concerned in this paper can be located, including two head noses of the trains encountering at t_1, the T2HN approaching T1-2 at t_2, the T2HN approaching T1-7 at t_3, the relative positions of the two vehicles coinciding at t_4, the T2TN leaving T1-2 at t_6, the T2TN leaving T1-7 at t_6, and two tail noses of the trains meeting at t_7. The time history pressure coefficient curve for this period measured by the probe P2-1 is shown in Fig. 9b. A significant positive pressure value occurs at t_2, which is caused by the head nose of train 2 squeezing the air as it passes the P1. Then, the pressure decreases rapidly to the minimum negative value as the air flows along the streamline of the head and accelerates. When the tail of train 2 leaves P2-1, the air accelerates along the streamline of the tail and then decelerates at the tail nose which induces a positive value at t_5. During the middle train of Train2 passing by Train1, several slight pressure fluctuations are observed at probe P2-1. To observe the pattern of pressure changes in each carriage, the C_{p_max}, C_{p_min}, and ΔC_p measured by the pressure probes on each carriage are extracted in Fig. 10. The pressure transition on the side of the streamlined head is slightly greater than that on the tail car, as shown in Fig. 10a. On $z=0.5H$ of the middle cars, the pressure transition is greater on the 2nd and 3rd cars, as shown in Fig. 10b. The magnitude of the pressure transition alternates with the marshalling location on the $z=0.19H$ of the train, the alternating pressure is strongest in the tail car, and the middle carriages show fluctuations in a tendency to decrease and then increase, as shown in Fig. 10c. The C_p distribution on the plane of $z=0.3H$ at t_1–t_7 moments is shown in Fig. 11. The positive and negative pressure zone induced by the head of the train is more significant than that induced by the tail of the train. There is a contraction in the positive pressure zones and expansion in the negative pressure zone near the head and tail region of the trains at the t_4 moment. To figure out the rule of pressure transit on the baseline of the equipment compartment region

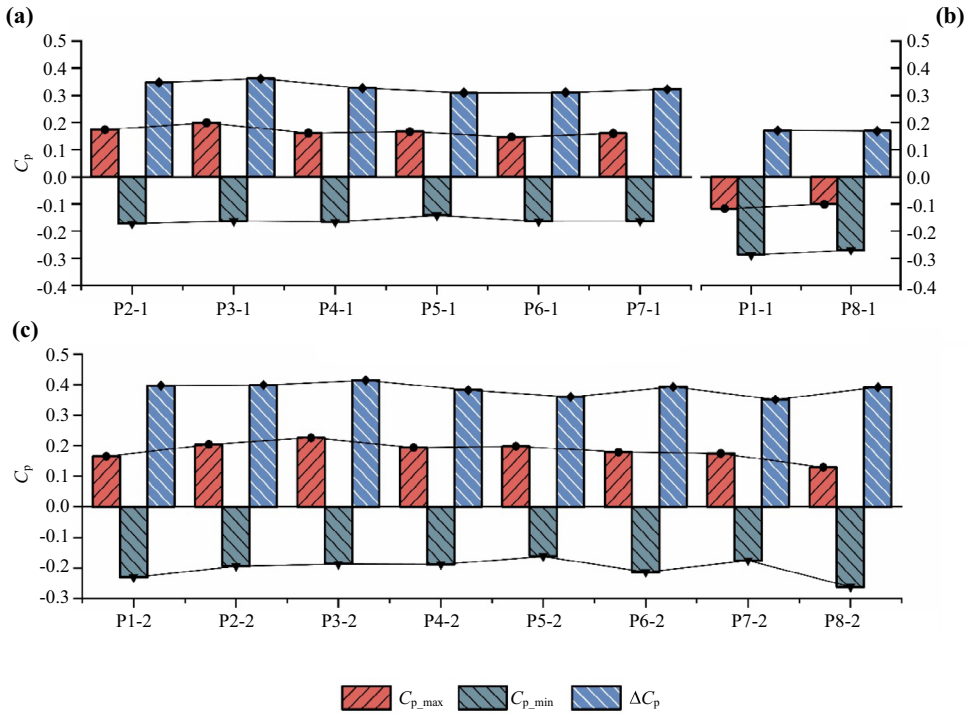

Fig. 10 Maximum, minimum, and peak–peak pressure coefficient values on **a** $z=0.5H$, **b** $z=0.82H$, and **c** $z=0.19H$

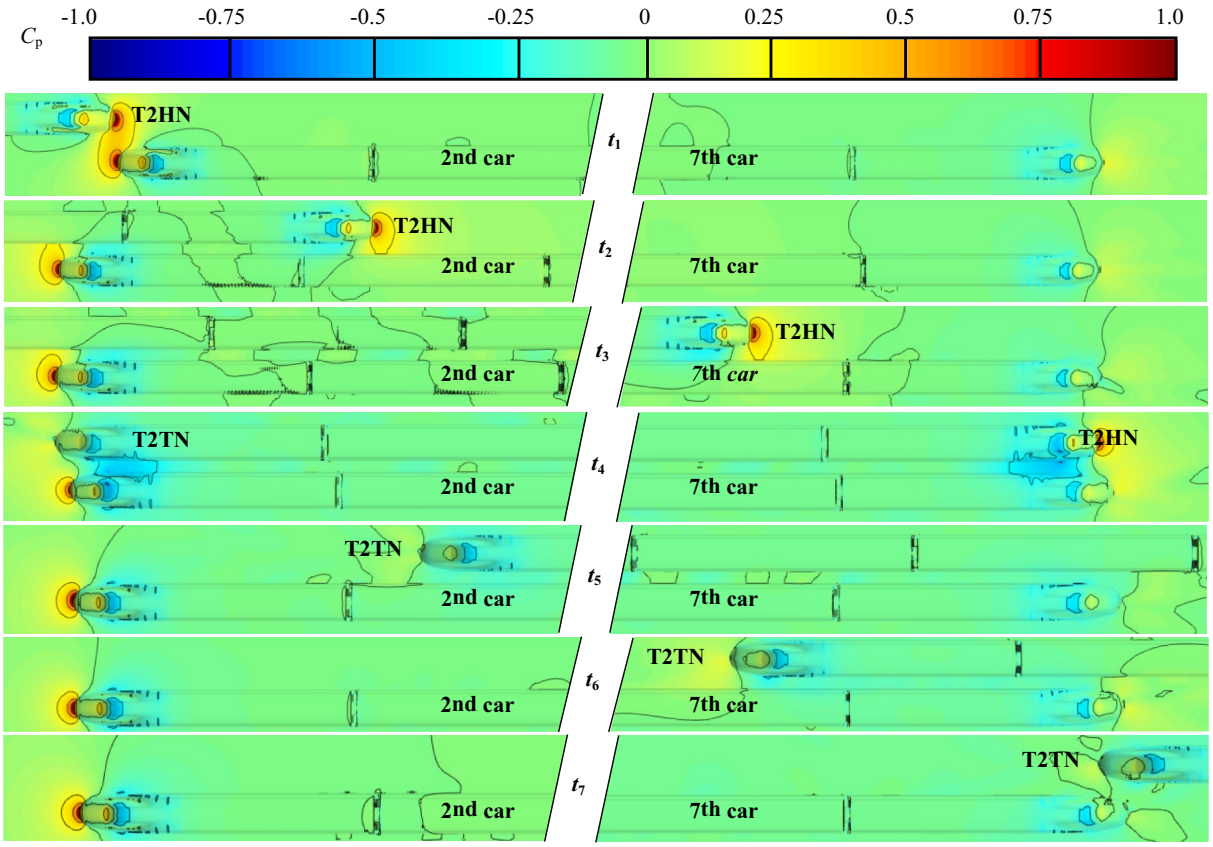

Fig. 11 C_p distribution on the train surface and the plane $z=0.3H$ at 7 special moments during the train meeting event

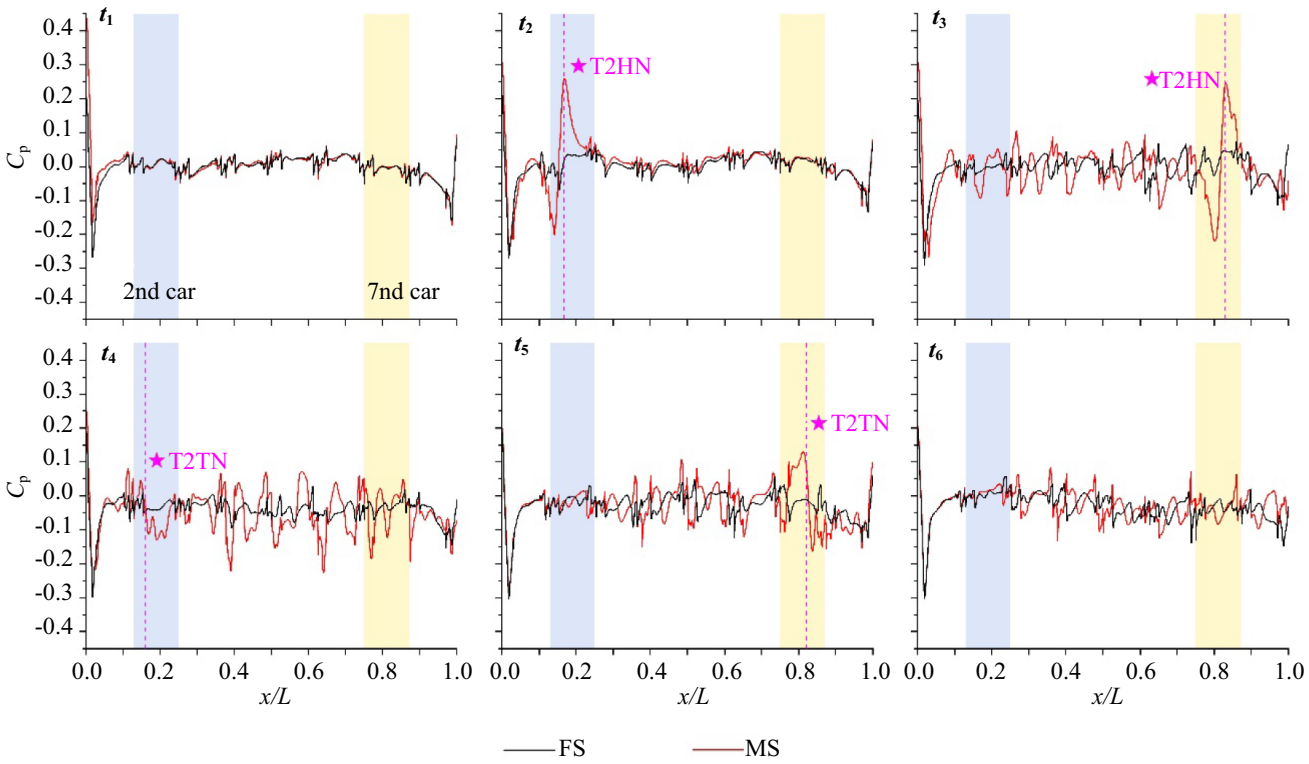

Fig. 12 C_p distribution on the meeting and free sides' (MS and FS) surface of equipment compartment region ($z=0.19H$) at 6 special moments during the train meeting event. The locations of T2HN and T2TN are highlighted by a pink dashed line

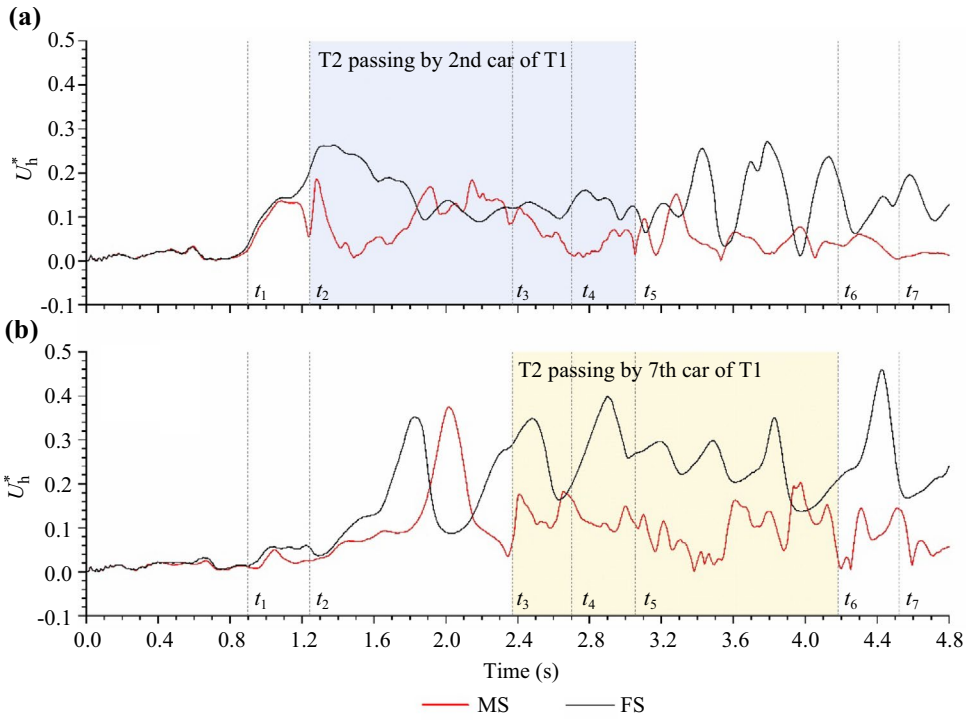

Fig. 13 Time history curves of U_h^* on two sides of **a** the 2nd car and **b** the 7th car

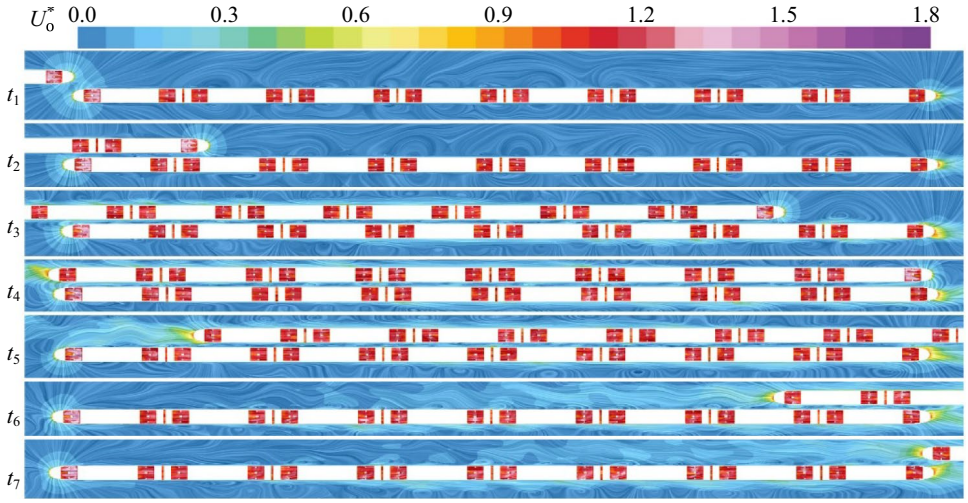

Fig. 14 U_o^* distribution on the plane $z=0.3H$ at 7 special moments during the train meeting event

($z=0.19H$) when the head car and tail car pass by, the C_p distributions at t_1, t_2, t_3, t_5, t_6, and t_7 are shown in Fig. 12. The 2nd car region and 7th car region are highlighted by the blue box and yellow box, respectively. When T2HN arrives, it causes the surface pressure of the equipment compartment to change from a negative pressure to a larger positive pressure, and this pressure difference is more significant when it passes through the 7th car, as shown in Fig. 12b and c. When T2TN leaves, it causes the surface pressure of the equipment compartment to change from a larger positive pressure to a negative pressure and induces greater fluctuations in the surface pressure of the equipment compartment compared with T2HN passes

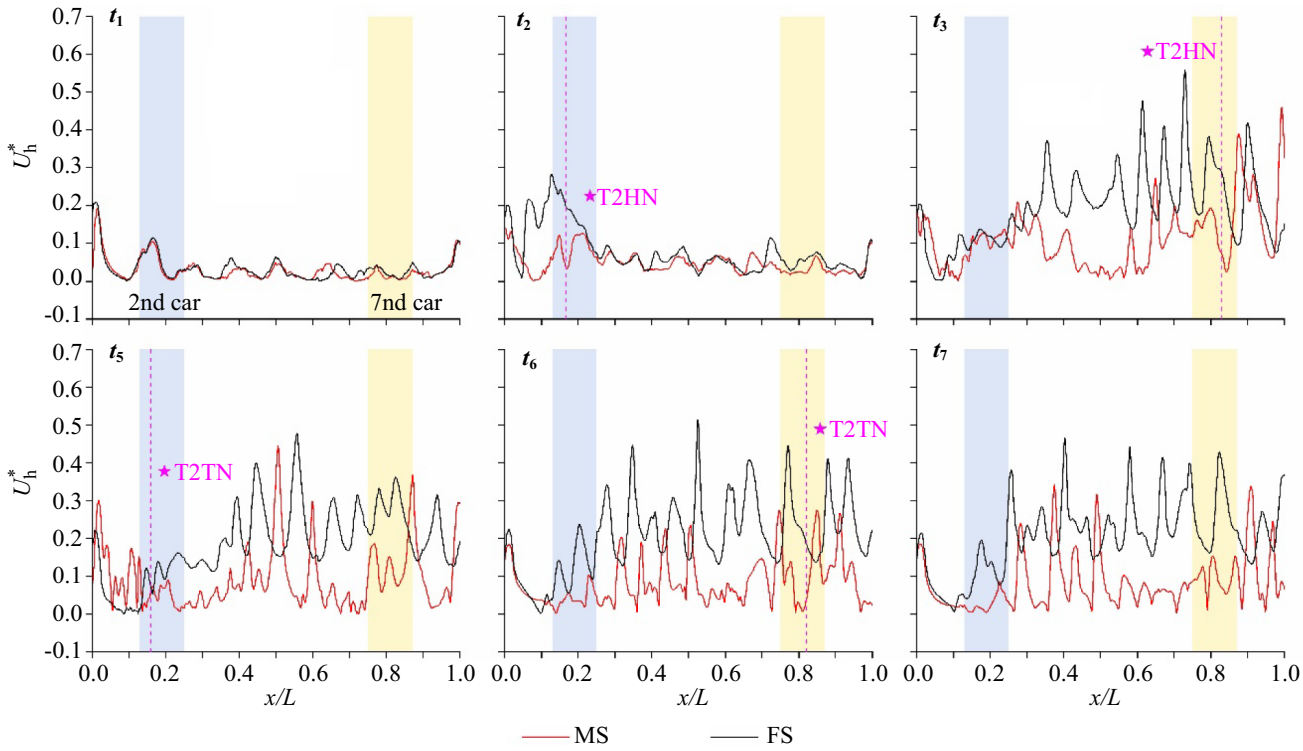

Fig. 15 U_h^* distribution on the baseline of cabin surface $z=0.19H$ at 6 special moments during the train meeting event. The locations of T2HN and T2TN are highlighted by a pink dashed line

by Train1, as shown in Fig. 12d and e. After the train meeting event, the great pressure fluctuations along the train surface still exist, as shown in Fig. 12a and f. In addition, the pressure transitions are more considerable on the meeting side than on the free side.

The time history curves of velocity in the horizontal plane (denoted as U_h^*) during the train meeting event are shown in Fig. 13. During train 2 passing by the 2nd car of train 1, the airflow velocity at the free side is former increased and pulled to the meeting side, and then drives the airflow velocity at the meeting side, as shown in Fig. 13a. The airflow velocity at two sides of Train1 rises and fluctuates before train 2 passes by the 7th car, as shown in Fig. 13b. When train 2 arrives, the airflow at the meeting side is squeezed and slows down. Then, the air flows from the free side to the meeting side, pushing the airflow velocity to increase. As the velocity magnitude U_o^* distribution on the plane of $z=0.3H$ at t_1–t_7 moments shown in Fig. 14, the head of the train has a minor effect on the disturbance of the surrounding airflow, while the tail wake has a significant effect on the disturbance of the surrounding airflow. The U_h^* distributions at t_1, t_2, t_3, t_5, t_6, and t_7 are shown in Fig. 15. When T2HN arrives, the airflow behind it at the free side responds first, and then, the airflow velocity at the meeting side increases, while the airflow in front of T2HN is squeezed and slowed down, as shown in Fig. 15b and c. When T2TN leaves, the airflow velocity behind it decreases, as shown in Fig. 15d. After the train meeting event, the significant velocity fluctuations along two sides of the train still exist, as shown in Fig. 15e and f. In addition, the velocity fluctuations are more considerable at the free side than at the meeting side, as it is constantly pushed to the meeting side.

3.3 Velocity inlet boundary condition

The velocity distributions on the inlet surface U_r^* near the 2nd car ($x=0.34L$) and 7th car ($x=0.96L$) for the train meeting period are input as velocity inlet of equipment compartment simulation, respectively, corresponding to NHC and NTC conditions. To ensure that the input data

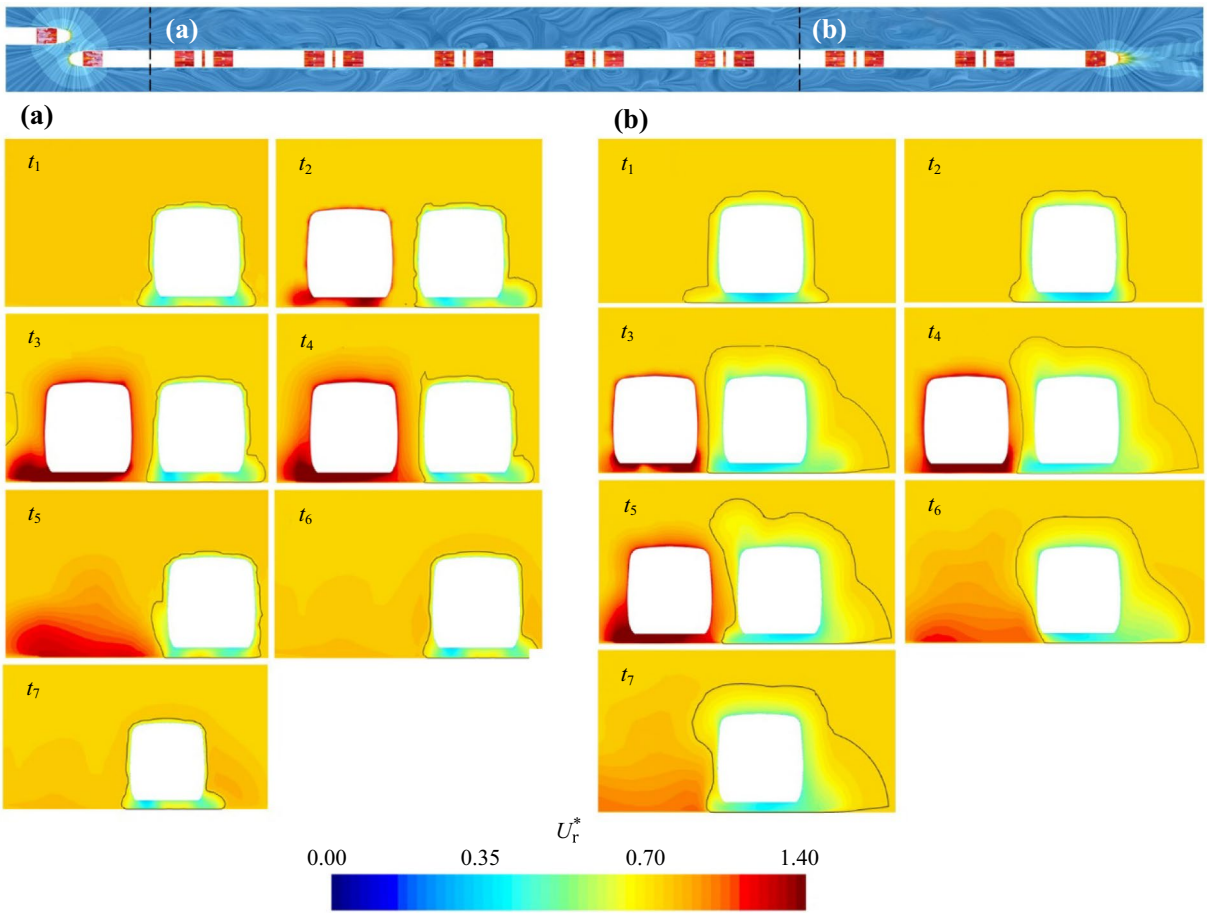

Fig. 16 U_r^* distribution on **a** the plane $x=0.34L$ and **b** $x=0.96L$ of train 1 at 7 special moments during the train meeting event. The black lines represent the outline of the low-speed area ($0.99U_r^*$)

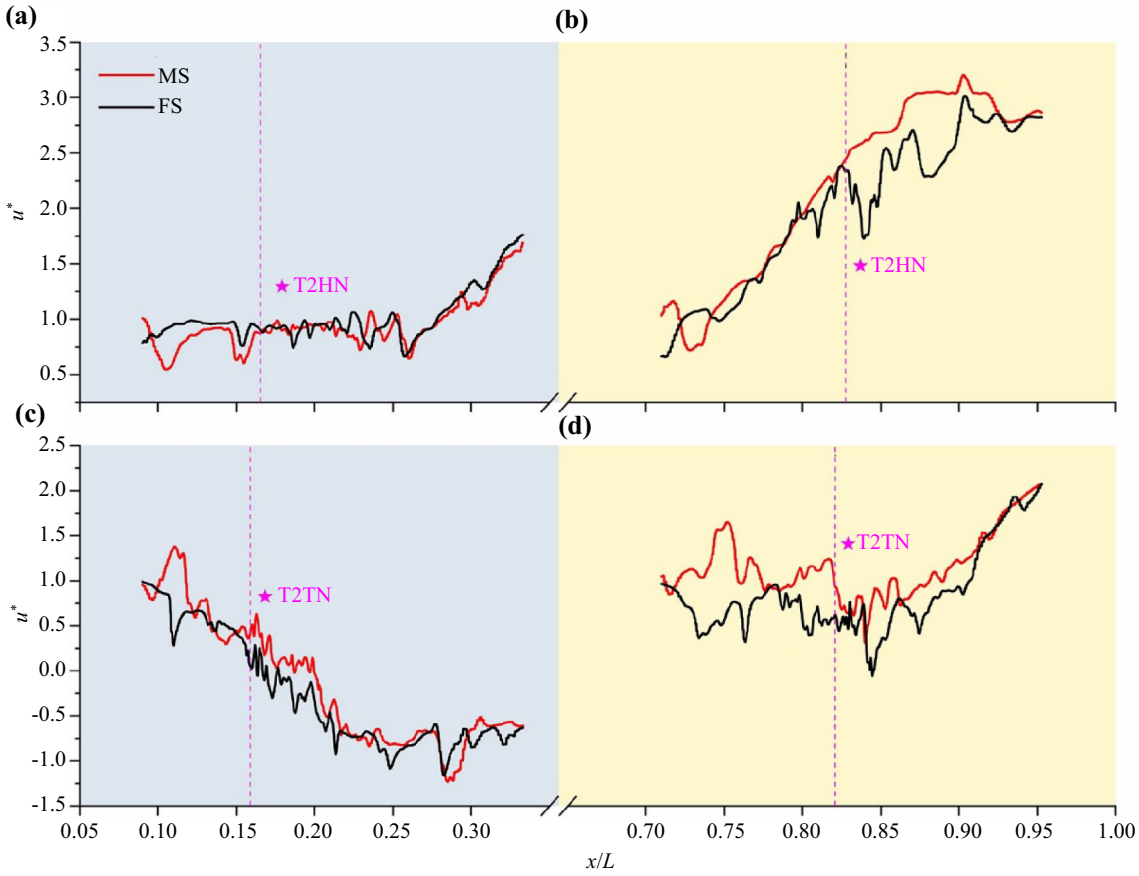

Fig. 17 u^* distribution of the equipment compartment on $y=0.68W$ and $y=-0.68W$ at **a** t_2 and **c** t_5 in the NHC condition and **b** t_3 and **d** t_6 in the NTC condition. The locations of T2HN and T2TN are highlighted by a pink dashed line

are continuous in time, the velocity at the corresponding position is zero when train 2 crosses the plane, and the boundary interpolates the transition with the surrounding flow field. The data input frequency are 2000 Hz. The U_r^* distributions on the inlet surface of NHC and NTC condition at t_1–t_7 moments are shown in Fig. 16. The flow velocity at the bottom of the train is greater and the velocity boundary layer is thicker around the train bogie than that around the train, due to the disturbing effect of the bogie. Comparing the velocity boundary layer at the same moment with Fig. 16a and b, the velocity boundary layer in the NTC condition is thicker than that in the NHC condition. During the train meeting event (at t_3–t_7), the velocity boundary layer is compressed between two trains, causing it to be thinner than the free sides of the two trains. Moreover, the boundary layer around the top of the train is thicker at the meeting side. As a result, the train meeting event will thicken the boundary layer, which might degrade the ventilation performance of equipment compartment.

3.4 Ventilation characteristic

The velocity distribution around the equipment compartment area and the air duct of converter, and the mass flow of the inlet side and outlet side of the air duct at t_2, t_5 in NHC condition (when T2HN arriving T1-2 and T2TN leaving T1-2) and t_3 and t_6 in NTC condition (when T2HN arriving T1-7 and T2TN leaving T1-7) are discussed in this section. The streamwise velocity u^* and vertical velocity v^* profiles along the inlet ($y=0.68W$) and outlet ($y=-0.68W$) sides of the equipment compartment are shown in Fig. 17 and Fig. 18. The u^* of the meeting side is slightly greater than that of the free side. When the T2HN reaches the equipment compartment of the 2nd car at t_2, the u^* and v^* are not affected (Fig. 17a and Fig. 18a). When it reaches the equipment compartment of the 7th car at t_3, the u^* in front of T2HN climbs rapidly up to around 3 times the train's operating speed (Fig. 17b). When the T2TN leaves the equipment compartment of the 2nd car at t_5, the airflow separates along the tail nose (Fig. 17c). When it leaves the equipment

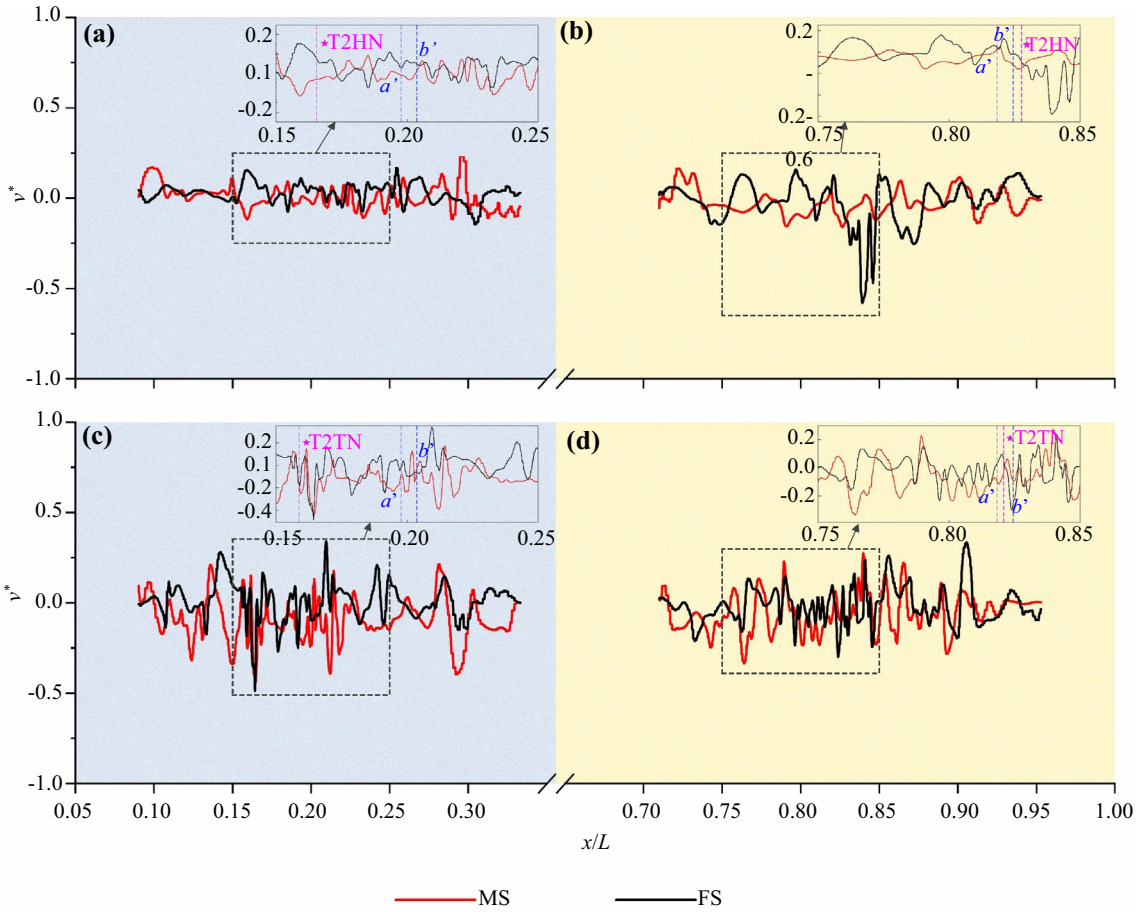

Fig. 18 v^* distribution of the equipment compartment on $y=0.68W$ and $y=-0.68W$ at **a** t_2 and **c** t_5 in the NHC condition and **b** t_3 and **d** t_6 in the NTC condition. The locations of T2HN and T2TN are highlighted by a pink dashed line. The middle of air duct 1 and air duct 2 of the converter are denoted as *a*' and *b*' and located with the blue dashed line

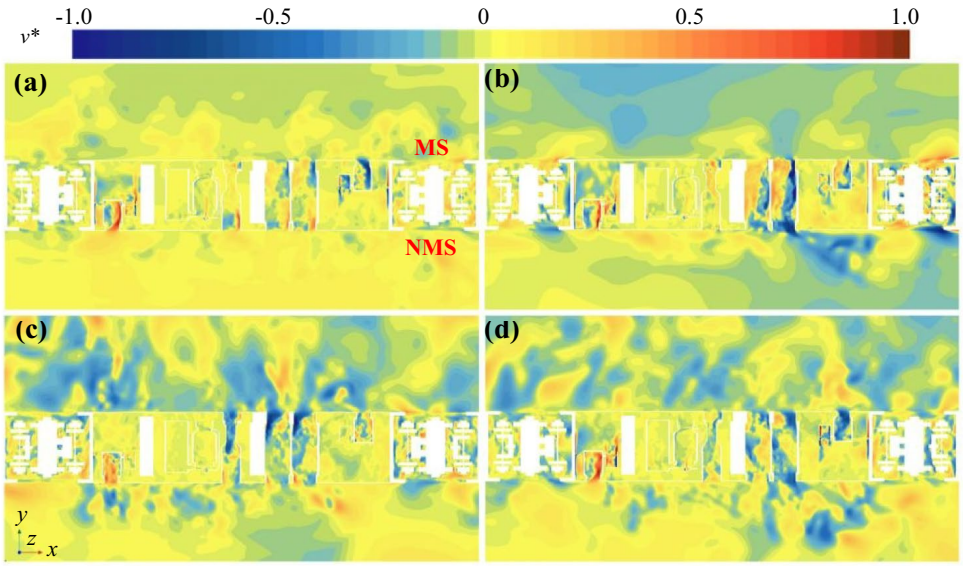

Fig. 19 v^* distribution of the equipment compartment on $z=0.19H$ at **a** t_2 and **c** t_5 in the NHC condition and **b** t_3 and **d** t_6 in the NTC condition

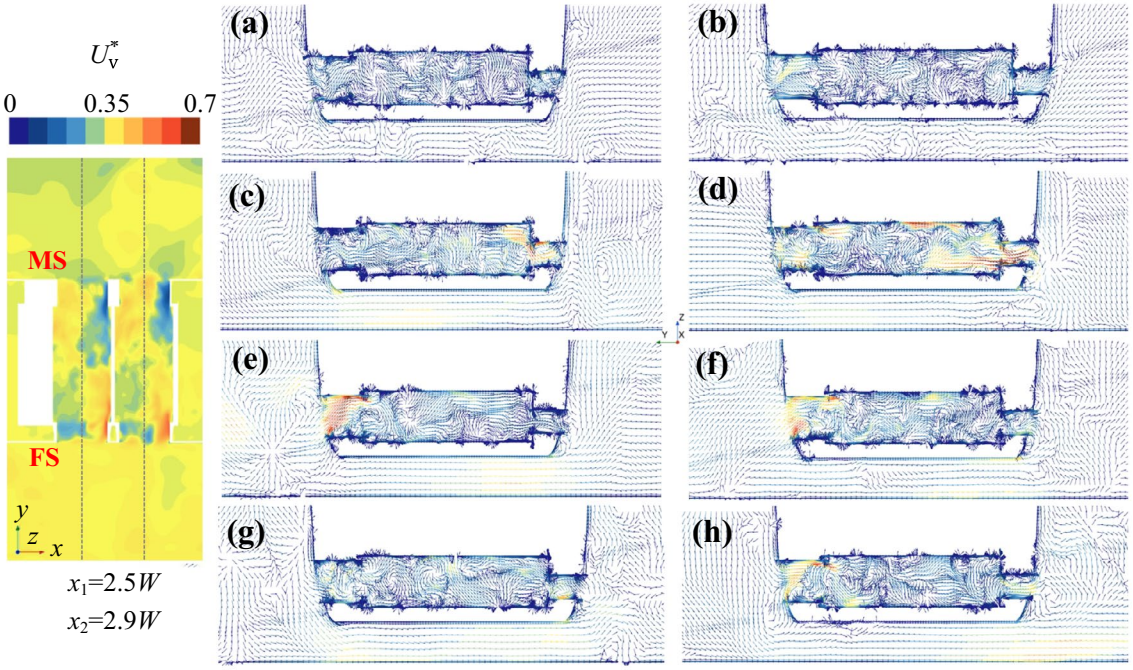

Fig. 20 U_y^* velocity vector image on the plane $x_1 = 2.5W$ at **a** t_2 and **e** t_5 in NHC condition and **c** t_3 and **g** t_6 in NTC condition; on the plane $x_1 = 2.9W$ at **b** t_2 and **f** t_5 in NHC condition and **d** t_3 and **h** t_6 in NTC condition

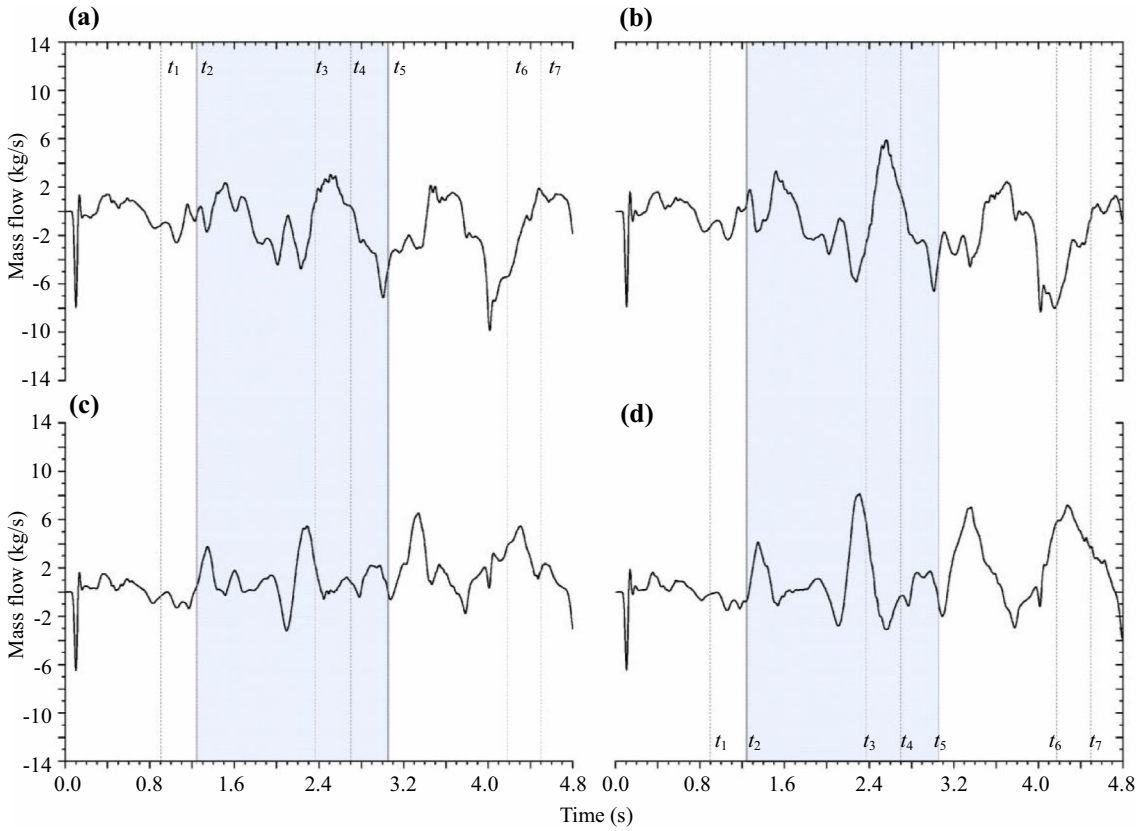

Fig. 21 Time history curves of mass flow in the inlets of **a** air duct 1 and **b** air duct 2, and the outlets of **c** air duct 1 and **d** air duct 2 in the NHC condition

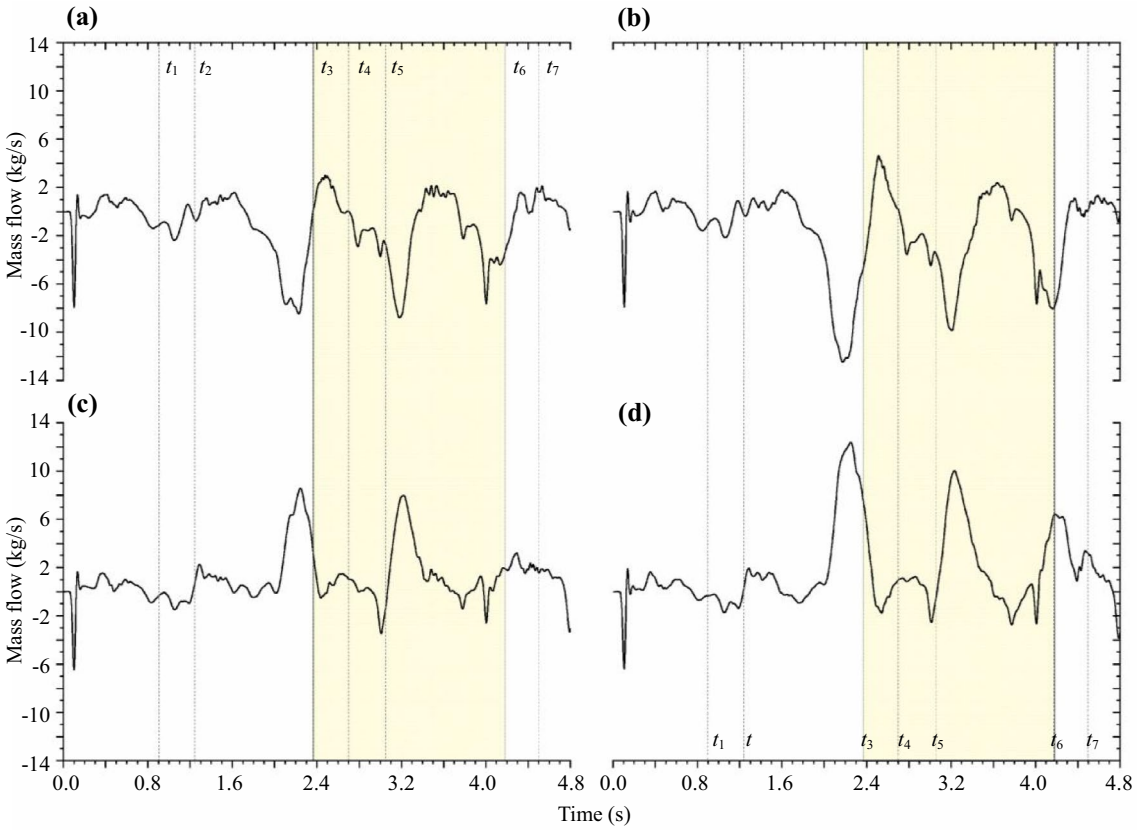

Fig. 22 Time history curves of mass flow in the inlets of **a** air duct 1 and **b** air duct 2, and the outlets of **c** air duct 1 and **d** air duct 2 in the NTC condition

compartment of the 7th car at t_6, the u^* in the wake of the tail nose rises (Fig. 17d).

The v^* distribution profiles along the equipment compartment are shown in Fig. 18. The difference in the v^* distribution of vents located at different locations along the train could be significant. Before the T2HN arrives at the converter of 2nd car, the air flows from the outlet vents (at the free side) to the inlet vents (at the meeting side), as shown in Fig. 18a. Before the T2TN leaves the converter of the 7th car, the air flows from the inlet vents to the outlet vents, as shown in Fig. 18c. When the T2HN passes the converter of 2nd car, the air flows to the meeting side in air duct 1 (*a*') and flows to the free side in air duct 2 (*b*'), as shown in Fig. 18b. When the T2TN reaches between two air ducts of the converter at the 7th car, the air flows in the air duct 1 from two vents and flows to the free side in air duct 2, as shown in Fig. 18d. The v^* distribution along the train fluctuates dramatically and frequently when Train2 leaves the equipment compartment. It promotes the air circulation rate of the duct. As shown by the v^* profiles in Fig. 19, as the T2HN arrives at the equipment compartment, it promotes the airflow towards the external environment for the vents. In contrast, it drives the airflow to enter the air duct for the vents when T2TN leaves. The flow characteristics inside the air duct of the converter were analysed. The velocity vectors in the vertical plane (denoted as U_v^*) embodied in the middle profile of the air duct 1 ($x_1 = 2.5W$) and air duct 2 ($x_2 = 2.9W$) are shown in Fig. 20. The ventilation performance of the air duct is considerably enhanced when T2HN reaches the 7th car of Train1, and the airflow exits the external environment at a greater rate. When T2TN leaves the 2nd car of train 1, the air duct is better ventilated than the T2TN leaves the 7th car of train 1 and the airflow is pushed into the air duct.

To analyse the ventilation performance rule for the train meeting period, the time history curves of mass flow in the inlet (at the meeting side) and outlet (at the free side) vent of the air ducts are shown in Figs. 21 and 22. The mass flow value is positive which means the airflow exhausts to the environment from vents located at the meeting side and enters the air ducts from vents located at the free side. On the contrary, the negative mass flow value means the airflow enters the air ducts from the meeting side and exhausts the environment from the free side. The blue box in Fig. 21 covers the period the train 2 arrives and leaves the equipment compartment in the 2nd car. As the T2HN approaches the vents, airflow is first pressed into the ducts from the meeting

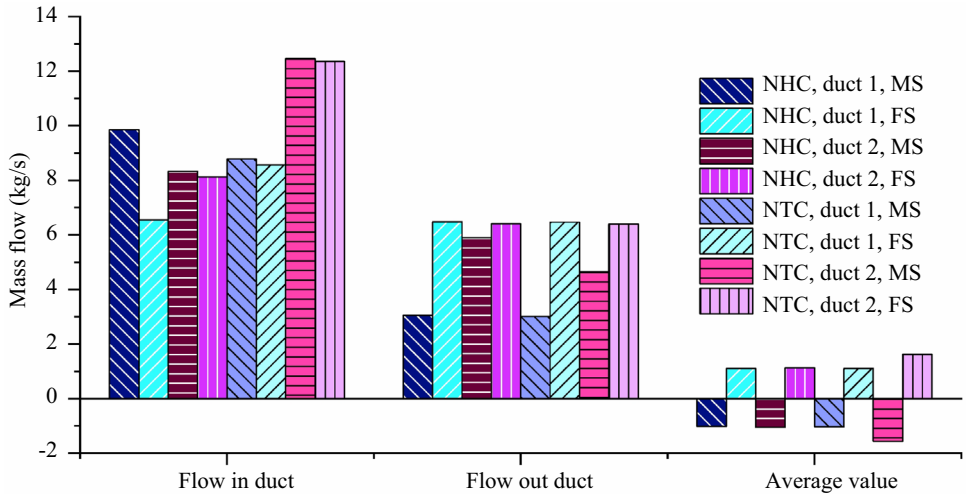

Fig. 23 Absolute maximum value and the absolute average value of mass flow in the meeting side and the free side of air ducts for the train meeting period

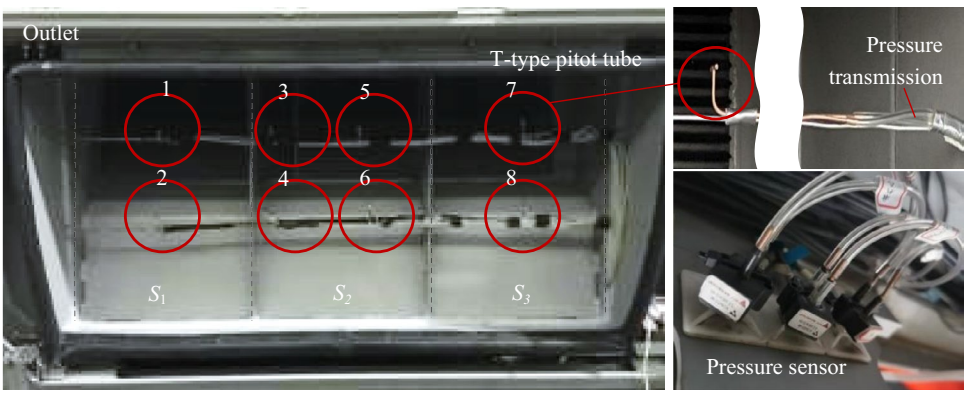

Fig. 24 TTPT test system diagram

side and then subsequently sucked out to the external environment from the free side to the meeting side. As the T2TN leaves the vents, airflow is pushed from the meeting side to the free side. The yellow box in Fig. 22 covers the period Train 2 arrives and leaves the equipment compartment in the 7th car. As the T2HN is close to the vents, airflow is drawn from the meeting and the free sides of the ducts to the external environment. As the T2TN leaves the vents, the airflow is first pushed from the meeting side to the free side, and then, it quickly switches from the free side to the meeting side.

The maximum and average values of the mass flow to and from the air ducts are listed in Fig. 23. The maximum mass flow that enters the air ducts from the meeting side is greater than that from the free side, with the maximum differential mass flow entering air duct 1 33.6%. While the maximum mass flow that discharges to the environment from the free side is considerably greater than that from the meeting side, the maximum differential mass flow exhaust to the environment from air duct 1 is 53%. The air is driven into the air ducts during the train meeting period, with the maximum ratio of the airflow in-duct to the airflow out-duct of 3.2. The average mass flow in the NTC condition is slightly greater than that in the NHC condition. Moreover, the average mass flow during the train meeting period is lower than the rated mass flow of the converter (1.3271 kg/s). The maximum inhibition ratio of average mass flow to the rated mass flow reaches − 23% in the inlet vent of air duct 1 in the NHC condition.

Moreover, the influence of the train meeting event on the ventilation performance should also be evaluated by comparing it with the single train running in the open air case. In Ref. [47], the average mass flow of the air duct 1 on

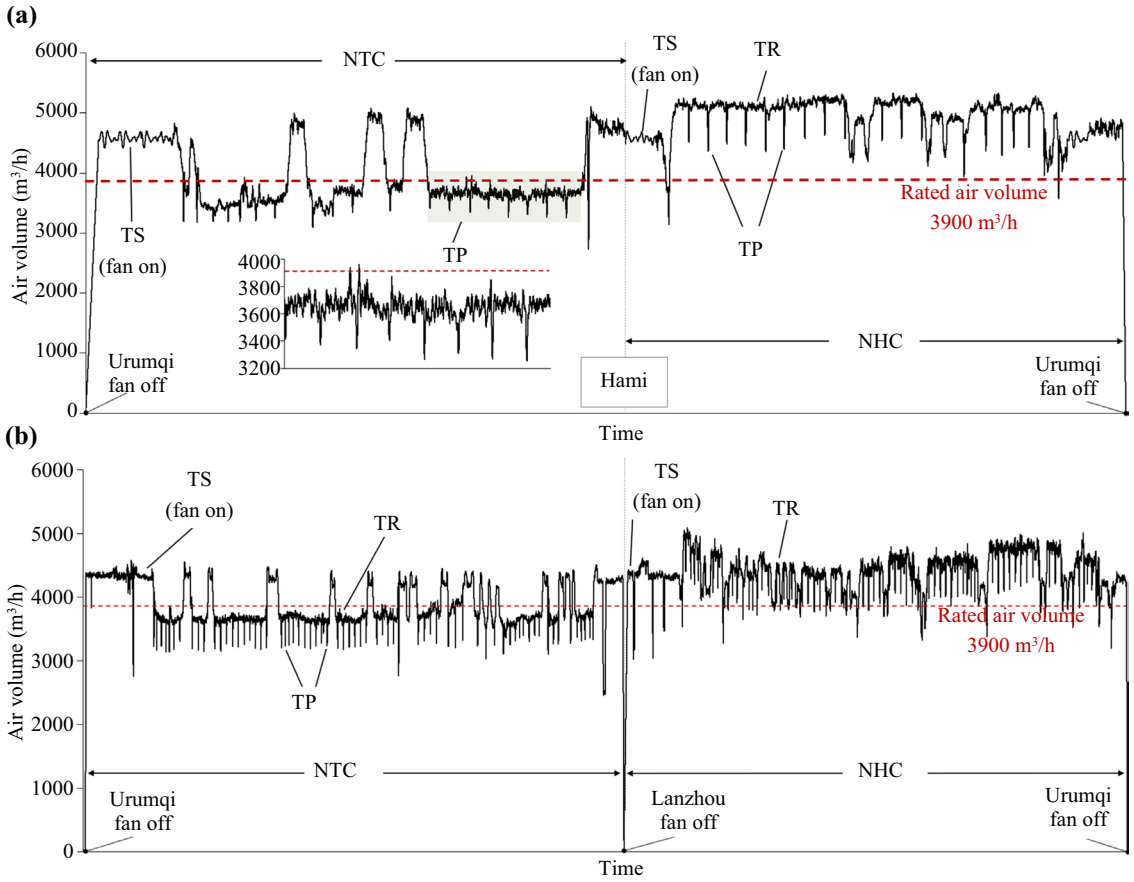

Fig. 25 Air volume of different running directions in **a** the Urumqi–Hami running route and **b** the Urumqi–Lanzhou running route

the free side in the NHC and NTC conditions is 1.354 and 1.221 kg/s, respectively. The inhibition ratios of the average mass flow in the train meeting event to the single-train operation in the NHC and NTC conditions are − 18% and − 9%.

4 Vehicle experiment on ventilation measurement

The Alpine HST operates between Urumqi–Hami–Lanzhou with a total length of 1,776 kms in north-western China, where the differential temperature in a day is so extreme that the electrical facilities are often alerted due to high temperatures. With the improvement in passenger and freight transport development in the northwest, the Lanxin Line became busier; meanwhile, train-passing events on this line became more frequent. Therefore, a real vehicle tracking test can contribute to monitoring the differences in the ventilation performance of electrical facilities under the single-train and train-passing scenarios. In this test, an 8-car train was operated at 200 km/h. The converter in the 2nd car was selected for the measurement subject, and the measurement points were arranged at its outlet vent 1.

As the train changed the running direction during the test, the relative location of the measurement subject was changed. When the train operates away from Urumqi, the 8th car will be the head car, and the measurement subject will be close to the tail car at this time (NTC condition), while the train approaches Urumqi, the 1st car is the head car, and the measurement subject will be close to the head car at this time (NHC condition).

4.1 Measurement method

A double heads *T*-type pitot tube (TTPT) is used in the real vehicle tests, which was developed by the key laboratory of traffic safety on track (Central South University). It is a symmetrical structure to meet the bi-directional flow measurement in the vehicle test, and its tubes are flexible to fit with the limited mounting space. In this case, 4 × 2 (rows × columns) measurement points have been mounted in the middle area of the vent to leave enough space for ventilation, as shown in Fig. 24. This arrangement method of measurement points is corrected based on the Chebyshev method in Ref. [47]; the correction factor is 0.882.

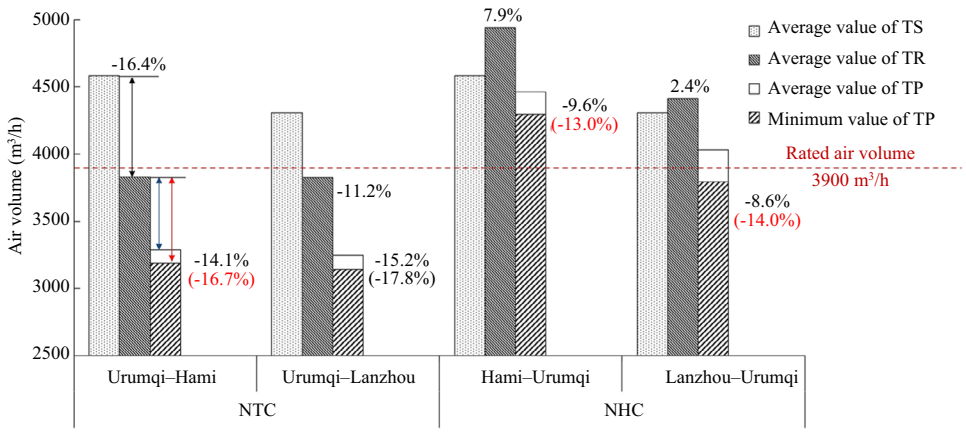

Fig. 26 Effect of train passing on air volume in different marshalling locations

The TTPT is connected to a differential pressure sensor using pressure transmission. According to the Bernoulli equation, the relationship of the differential pressure between two pressure holes of TTPT and the airflow velocity is given:

$$\Delta P_{\mathrm{d}} = \frac{1}{2}\rho V_{\mathrm{m}}^2, \tag{2}$$

where ΔP_{d} is the dynamic pressure (Pa) and V_{m} is measured airflow velocity (m/s).

The air volume Q (m^3/h) at the outlet vent cross section is obtained:

$$Q = \frac{\left(V_{\mathrm{m1}} + V_{\mathrm{m2}}\right)}{2} \cdot S_1 + \frac{\left(V_{\mathrm{m3}} + V_{\mathrm{m4}} + V_{\mathrm{m5}} + V_{\mathrm{m6}}\right)}{4} \cdot S_2 + \frac{\left(V_{\mathrm{m7}} + V_{\mathrm{m8}}\right)}{2} \cdot S_3, \tag{3}$$

where $V_{\mathrm{m}i}$ is the velocity of each measurement point (m/s) and S is the area of the air outlet vent cross section (m).

4.2 Results analysis on running conditions

The air volume of different running locations in different operating routes during the test cycle is shown in Fig. 25. For analysing the ventilation performance in different running locations, the test data during the single-train stationary condition (TS), the single-train operation condition (TR), and train-passing events (TP) were picked out according to the operating mileage logs. The fans inside the air duct in the three operating conditions above are on. As shown in Fig. 26, in TS conditions, the averaged air volumes of the air outlet when the train runs on the route Urumqi–Hami and Urumqi–Lanzhou are 4,580 and 4,304 m^3/h, respectively, which are higher than the rated air volume 3,900 m^3/h to meet the normal working requirements of the equipment. When in the TR event, the average air volumes of the converter in the NHC condition on the route of Hami–Urumqi and Lanzhou–Urumqi are 4,940 and 4,409 m^3/h, which is 7.9% and 2.4% higher than the static air volume, respectively. While in NTC conditions, the average air volumes of the converter on the route of Hami–Urumqi and Lanzhou–Urumqi are 3,828 and 3,822 m^3/h, in other words, the restraint ratios in contrast to the static air volume are − 16.4% and − 11.2%, respectively, which is close to or even lower than the rated air volume 3,900 m^3/h. During the TP period, which causes suppression in the average air volume, especially during the NTC conditions, the air volume is below the rated air volume of 3,900 m^3/h. The average air volumes on the route of Hami–Urumqi and Lanzhou–Urumqi are 4,464 and 4,030 m^3/h in the NHC condition. The reduction ratios relative to the single-train condition are − 9.6% and − 8.6%, respectively. In the NTC condition, the average air volumes are 3,288 and 3,250 m^3/h. The reduction ratios relative to the single-train condition are − 14.1% and − 15.0%, respectively.

4.3 Results comparison between simulation and experiment

For comparing the average air volume of the simulation and the real vehicle test, they are normalised as in Eq. (4) and (5).

$$c_{\mathrm{q\_sim}} = \frac{Q_{\mathrm{TP}}}{Q_{\mathrm{rated}}} = \frac{3,600M/\rho}{Q_{\mathrm{rated}}}, \tag{4}$$

$$c_{\mathrm{q\_test}} = \frac{Q_{\mathrm{TP}}}{Q_{\mathrm{rated}}} / \frac{Q_{\mathrm{static}}}{Q_{\mathrm{rated}}} = \frac{Q_{\mathrm{TP}}}{Q_{\mathrm{static}}}, \quad (5)$$

where the average air volume during the train is static (fans are working), train-passing event, and the rated air volume of the ventilation equipment's cooling fan is denoted as Q_{static}, Q_{TP}, and Q_{rated} (m^3/h), respectively. M is the mass flow (kg/s).

The air volume coefficient of the outlet vent 1 in the vehicle test on the route of Lanzhou–Urumqi in NHC and NTC conditions is 0.936 and 0.755, respectively. The air volume coefficient of the outlet vent 1 in the simulations in NHC and NTC conditions is 0.832 and 0.836, respectively. The air volume coefficient reflects the reduction rate of ventilation performance during the train meeting event relative to the normal state. The maximum reduction rate of the test and simulation are − 24.5% and − 16.8%. Consistently, the ventilation performance of the electrical facilities is suppressed during the train meeting period. The deviation ratios between the test and simulation in the NTC and NHC conditions are 12.5% and − 9.7%. The ambient wind is not considered in the simulation, while the vehicle test was performed on the Lanxin Line in windy weather. Ambient wind can affect the measurement results of airflow. Although the error satisfies the engineering requirement, the effect of ambient winds should be considered when processing the results of measuring equipment ventilation in future research.

5 Conclusions

To accommodate the increasing frequency of train meeting events in the future, the effect of the train meeting event on the ventilation performance of equipment was investigated through a two-step numerical simulation. In addition, a real vehicle tracking test was conducted using TTPT.

Conclusions for the numerical calculation are as follows:

1. Based on the analysis of the external flow field, it is assumed that the dominant factor affecting the ventilation effect when the head arrives at the equipment compartment is the positive pressure area formed by the head nose squeezing the airflow and resulting in the airflow slowing down. The dominant factor affecting the ventilation effect when the tail leaves is the large turbulence energy caused by the tail wake resulting in an unstable status.
2. The train meeting event will result in a thickening of the boundary layer around the train, which is not conducive to the ventilation of the equipment compartment.
3. The air is driven into the air ducts during the train meeting period, with the maximum ratio of the airflow induct to the airflow out-duct of 3.2.
4. The average mass flow during the train meeting period is lower than the rated mass flow of the converter (1.3271 kg/s). The maximum inhibition ratio of average mass flow to the rated mass flow reaches − 23%.
5. The inhibition ratios of the average mass flow in the train meeting event to the single-train operation in the NHC and NTC conditions are − 18% and − 9%.

Conclusions for the real vehicle test are as follows:

i. During the train meeting period, the average air volumes on the route of Hami–Urumqi and Lanzhou–Urumqi are 4,464 and 4,030m^3/h in the NHC condition, which is − 9.6% and − 8.6% lower than the single-train condition, respectively. In the NTC condition, the average air volumes are 3,288 and 3,250 m^3/h, which is − 14.1% and − 15.0% lower than the single-train condition, respectively.
ii. The ventilation performance of the electrical facilities is suppressed during the train meeting period.

In the future, the influence of trains passing through the tunnel and meeting inside the tunnel on the ventilation performance of equipment compartment will be considered. Besides, the effect of ambient winds should be considered when processing the airflow test results measured by TTPT.

Acknowledgements The authors gratefully acknowledge the financial support by Technology R&D Program of China State Railway Group Co., Ltd (Grant number N2022J013), the Hunan Provincial Innovation Foundation for Postgraduate (Grant number CX20220279), the Fundamental Research Funds for the Central Universities of Central South University (Grant number 2022ZZTS0193), and China Scholarship Council (202106370112). The authors thank Mr. Shengqiang Chen for his assistance in programming. This work was carried out in part using computing resources at the High-Performance Computing Centre of Central South University and SNIC (Swedish National Infrastructure for Computing) at National Supercomputer Center (NSC).

References

1. Fujii K, Ogawa T (1995) Aerodynamics of high-speed trains passing by each other. Comput Fluids 24(8):897–908

2. Chen Y, Wu Q (2018) Study on unsteady aerodynamic characteristics of two trains passing by each other in the open air. J Vibroeng 20(2):1161–1178
3. Hermanns L, Giménez JG, Alarcón E (2005) Efficient computation of the pressures developed during high-speed train passing events. Comput Struct 83(10–11):793–803
4. Srivastava S, Sivasankar G, Dua G (2022) A review of research into aerodynamic concepts for high speed trains in tunnels and open air and the air-tightness requirements for passenger comfort. Proc Inst Mech Eng Part F J Rail Rapid Transit 236(9):1011–1025
5. Du J, Zhang L, Yang M et al (2020) Moving model experiments on transient pressure induced by a high-speed train passing through noise barrier. J Wind Eng Ind Aerodyn 204:104267
6. Liu Y, Yang W, Deng E et al (2023) Aerodynamic impacts of high-speed trains on city-oriented noise barriers: a moving model experiment. Alex Eng J 68:343–364
7. Meng S, Zhou D, Xiong X et al (2022) The effect of the nose length on the aerodynamics of a high-speed train passing through a noise barrier. Flow Turbul Combust 108(2):411–431
8. Li C, Liu M, Chang R et al (2022) Air pressure and comfort study of the high-speed train passing through the subway station. Sustain Cities Soc 81:103881
9. Liang X, Chen G, Li X et al (2020) Numerical simulation of pressure transients caused by high-speed train passage through a railway station. Build Environ 184:107228
10. Zhou D, Tian H, Zhang J et al (2014) Pressure transients induced by a high-speed train passing through a station. J Wind Eng Ind Aerodyn 135:1–9
11. Zhou D, Li J, Li X et al (2023) Experimental study on ventilation shaft locations for alleviating transient pressure induced by high-speed trains passing through underground station. J Cent South Univ 30(7):2427–2440
12. Meng S, Li X, Chen G et al (2021) Numerical simulation of slipstreams and wake flows of trains with different nose lengths passing through a tunnel. Tunn Undergr Space Technol 108:103701
13. Wang Q, Hu Z, Liang X et al (2023) Experimental simulation of alternating aerodynamic loads induced by high-speed trains passing in tunnels. Proc Inst Mech Eng Part F J Rail Rapid Transit 237(9):1176–1184
14. Zhao J, Li R (2011) A study of aerodynamic effects of high-speed trains through tunnels. Appl Mech Mater 94–96:1663–1667
15. C Baker, M Sterling (2004) The effects of the slipstreams of passing high speed trains on waiting passengers. In: Wind Engineering Society Conference, Cranfield
16. S C Jordan (2008) An investigation of the slipstreams and wakes of trains and the associated effects on trackside people and objects. Dissertation, University of Birmingham
17. Hu H, Xiang H, Liu K et al (2022) Aerodynamic characteristics of moving vehicles of two trains passing each other on bridge under crosswinds. J Cent South Univ 29(8):2558–2573
18. Zhao Y, Zhang J, Li T et al (2012) Aerodynamic performances and vehicle dynamic response of high-speed trains passing each other. J Mod Transp 20(1):36–43
19. Liu T, Chen Z, Zhou X et al (2018) A CFD analysis of the aerodynamics of a high-speed train passing through a windbreak transition under crosswind. Eng Appl Comput Fluid Mech 12(1):137–151
20. Wu H, Zhou Z (2017) Study on aerodynamic characteristics and running safety of two high-speed trains passing each other under crosswinds based on computer simulation technologies. J Vibroeng 19(8):6328–6345
21. Ouyang D, Deng E, Ni Y et al (2023) Evolution of flow field around high-speed trains meeting at the tunnel entrance under strong wind-rain environments. J Wind Eng Ind Aerodyn 241:105537
22. Chen X, Liu T, Zhou X et al (2017) Analysis of the aerodynamic effects of different nose lengths on two trains intersecting in a tunnel at 350 km/H. Tunn Undergr Space Technol 66:77–90
23. Li F, Luo J, Wang D et al (2022) Aerodynamic characteristics when trains pass each other in high-speed railway shield tunnel. Appl Sci 12(12):6244
24. Zhang M, Yang Y, Lu L et al (2012) Numerical simulation of two high speed trains passing by each other in a long tunnel. Appl Mech Mater 117–119:670–673
25. Sun Z, Zhang Y, Guo D et al (2014) Research on running stability of CRH3 high speed trains passing by each other. Eng Appl Comput Fluid Mech 8(1):140–157
26. Raghunathan RS, Kim HD, Setoguchi T (2002) Aerodynamics of high-speed railway train. Prog Aerosp Sci 38(6–7):469–514
27. Huang S, Li Z, Yang M (2019) Aerodynamics of high-speed maglev trains passing each other in open air. J Wind Eng Ind Aerodyn 188:151–160
28. Xia Y, Liu T, Wang X et al (2023) Piecewise linear representation of pressure wave data of high-speed trains traveling through tunnels. J Cent South Univ 30(7):2411–2426
29. Tian H, He H (2005) Influence of various factors on the air pressure pulse from passing trains. Int J Heavy Veh Syst 12(1):60–68
30. Baker C, Jordan S, Gilbert T et al (2014) Transient aerodynamic pressures and forces on trackside and overhead structures due to passing trains. Part 1: Model-scale experiments; Part 2: Standards applications. Proc Inst Mech Eng Part F J Rail Rapid Transit 228(1):37–70
31. Liu T, Chen X, Li W et al (2017) Field study on the interior pressure variations in high-speed trains passing through tunnels of different lengths. J Wind Eng Ind Aerodyn 169:54–66
32. Schwanitz S, Wittkowski M, Rolny V et al (2013) Pressure variations on a train–Where is the threshold to railway passenger discomfort? Appl Ergon 44(2):200–209
33. Peng Y, Fan C, Hu L et al (2019) Tunnel driving occupational environment and hearing loss in train drivers in China. Occup Environ Med 76(2):97–104
34. Wang T, Wu F, Yang M et al (2018) Reduction of pressure transients of high-speed train passing through a tunnel by cross-section increase. J Wind Eng Ind Aerodyn 183:235–242
35. Sun Z, Yang G, Zhu L (2014) Study on the critical diameter of the subway tunnel based on the pressure variation. Sci China Technol Sci 57(10):2037–2043
36. Hwang J, Yoon T, Lee D et al (2001) Numerical study of unsteady flowfield around high speed trains passing by each other. JSME Int J, Ser B 44(3):451–464
37. Hwang J, Lee DH (1999) Numerical simulation of flowfield around high speed trains passing by each other. In: the 17th Applied Aerodynamics Conference. Norfolk, pp 3156
38. Li W, Liu T, Chen Z et al (2020) Comparative study on the unsteady slipstream induced by a single train and two trains passing each other in a tunnel. J Wind Eng Ind Aerodyn 198:104095
39. Meng S, Meng S, Wu F et al (2021) Comparative analysis of the slipstream of different nose lengths on two trains passing each other. J Wind Eng Ind Aerodyn 208:104457
40. Yi L, Li Y, Ouyang J et al (2022) Modeling and simulation analysis of the temperature field of high speed missile cabin. J Phys: Conf Ser 2179(1):012007
41. Wang C, Xu R, Jiang P (2024) Numerical study on spray cooling of aircraft equipment cabin. Appl Therm Eng 239:122086
42. Niu J, Zheng Q, Lv D et al (2022) Numerical simulation of the effect of air-intake on the indoor flow field of a dedusting equipment cabin used in tunnel construction. Alex Eng J 61(12):12405–12416

43. Jia Q, Xia C, Zang J et al (2016) Numerical simulation on the temperature field in an equipment cabin of a high-speed railway train. Build Simul 9(6):689–700
44. Zhang N, Lu Z, Niu J et al (2017) Temperature field in equipment cabin of high-speed train in the harsh wind environment and extreme temperature condition. DEStech Trans Eng Technol Res 2017:903–910
45. Li X, Wu F, Tao Y et al (2019) Numerical study of the air flow through an air-conditioning unit on high-speed trains. J Wind Eng Ind Aerodyn 187:26–35
46. Li X, Wu F, Tao Y et al (2022) Numerical investigation of flow deflectors for the improvement of condensing air flux through the air-conditioning unit on high-speed trains. Build Environ 215:108949
47. Wu Y, Zhou W, Liang X et al (2023) Numerical and experiment study on ventilation performance of the equipment compartment of Alpine high-speed train. Eng Appl Comput Fluid Mech 17(1):2252514
48. Jiang Z, Liu T, Chen X et al (2019) Numerical prediction of the slipstream caused by the trains with different marshalling forms entering a tunnel. J Wind Eng Ind Aerodyn 189:276–288
49. Tan C, Zhou D, Chen G et al (2020) Influences of marshalling length on the flow structure of a maglev train. Int J Heat Fluid Flow 85:108604
50. Huang Y, Hong TH, Kim CN (2012) A numerical simulation of train-induced unsteady airflow in a tunnel of Seoul subway. J Mech Sci Technol 26(3):785–792
51. Cheng F, Xiong X, Tang M et al (2022) Impact of the gap distance between two adjacent external windshields of a high-speed train on surrounding flow characteristics: an IDDES study. Eng Appl Comput Fluid Mech 16(1):724–745
52. Dong T, Minelli G, Wang J et al (2022) Numerical investigation of a high-speed train underbody flows: studying flow structures through large-eddy simulation and assessment of steady and unsteady Reynolds-averaged Navier-Stokes and improved delayed detached eddy simulation performance. Phys Fluids 34(1):015126
53. He K, Su X, Gao G et al (2022) Evaluation of LES, IDDES and URANS for prediction of flow around a streamlined high-speed train. J Wind Eng Ind Aerodyn 223:104952
54. Xia C, Wang H, Shan X et al (2017) Effects of ground configurations on the slipstream and near wake of a high-speed train. J Wind Eng Ind Aerodyn 168:177–189
55. Foster A, Kinzel M (2021) Estimating COVID-19 exposure in a classroom setting: a comparison between mathematical and numerical models. Phys Fluids 33(2):021904
56. Su X, He K, Xu K et al (2023) Comparison of flow characteristics behind squareback bluff-bodies with and without wheels. Phys Fluids 35(3):035114
57. Zhang J, Guo Z, Han S et al (2022) An IDDES study of the near-wake flow topology of a simplified heavy vehicle. Transp Saf Environ 4(2): tdac015
58. Zhang J, Gidado F, Adamu A et al (2023) An investigation on the wake flow of a generic ship using IDDES: the effect of computational parameters. Ocean Eng 271:113644
59. Shur ML, Spalart PR, Strelets MK et al (2008) A hybrid RANS-LES approach with delayed-DES and wall-modelled LES capabilities. Int J Heat Fluid Flow 29(6):1638–1649
60. Chu CR, Chien SY, Wang CY et al (2014) Numerical simulation of two trains intersecting in a tunnel. Tunn Undergr Space Technol 42:161–174
61. Anderson J (2011) Fundamentals of aerodynamics, 7th edn. McGraw Hill, New York
62. Liu K, Jing L, Ren M (2018) The characteristics of air wave induced by two high-speed trains passing by each other in a tunnel. Adv Mech Eng 10(3):1–16
63. Zhang S (2007) CRH2 electric multiple unit. China Railway Publishing House Co., Ltd, Beijing (in Chinese)
64. Cheng N, Hao Z, Tan S (2008) Comparison of quadratic and power law for nonlinear flow through porous media. Exp Therm Fluid Sci 32(8):1538–1547
65. M Ariff, SM Salim, SC Cheah (2009) Wall $y+$ approach for dealing with turbulent flow over a surface mounted cube: Part 2—High Reynolds Number. In: Seventh International Conference on CFD in the Mineral and Process Industries, Melbourne, pp 1–6
66. Dong T, Liang X, Krajnović S et al (2019) Effects of simplifying train bogies on surrounding flow and aerodynamic forces. J Wind Eng Ind Aerodyn 191:170–182
67. Xiong X, Liang X (2009) Analysis of air pressure pulses in meeting of CRH2 EMU trains. J Chin Railw Soc 31(6):15–20 (in Chinese)